INTERNATIONAL JOURNAL OF CLIMATOLOGY
Int. J. Climatol. **37** (Suppl.1): 476–496 (2017)
Published online 16 March 2017 in Wiley Online Library
(wileyonlinelibrary.com) DOI: 10.1002/joc.5016

RMetS
Royal Meteorological Society

Evaluation of intra-seasonal oscillation simulations in IPCC AR5 coupled GCMs associated with the Asian summer monsoon

Wenting Hu,[a,b]* Anmin Duan[a] and Bian He[a]

[a] *State Key Laboratory of Numerical Modeling for Atmospheric Sciences and Geophysical Fluid Dynamics, Institute of Atmospheric Physics, Chinese Academy of Sciences, Beijing, China*

[b] *Key Laboratory of Meteorological Disaster of Ministry of Education, Nanjing University of Information Science and Technology, Nanjing, China*

ABSTRACT: In this study, we systematically evaluate the intra-seasonal oscillation (ISO) associated with the Asian summer monsoon region in coupled general circulation models (GCMs) participating in the Intergovernmental Panel on Climate Change (IPCC) Fifth Assessment Report (AR5). Results show that most of the models simulate reasonable climatological circulation patterns in boreal summer, but insufficient precipitation over the Bay of Bengal (BOB) and western North Pacific summer monsoon region. Most models underestimate the variance of 12–90-day ISO mode but overestimate the percent variance of 12–90-day ISO accounting for raw precipitation anomalies. There remains a wide gap between model simulations and observations in the simulations of eastward-propagating ISO (30–80-day), while the models perform better in the northward propagation of the 30–80-day mode and the westward propagation of the 12–24-day mode.

In addition, mean state circulation, atmospheric internal dynamic process, air–sea interactions and model resolution have varying degrees of impacts on the ISO simulation. The local Hadley and Walker cell biases are investigated in this study, which might relate well with the precipitation bias in models. Within the similar background of vertical easterly shear, few models have the capacity to simulate the equivalent barotropic vorticity to the north of the convection centre. Furthermore, many models have difficulty in reproducing the strong air–sea interactions over the Indian Ocean and the BOB. Our results indicate that simply improving model resolution is not an effective method to obtain more reasonable propagation characteristics of the ISO, especially for eastward propagation. Therefore, further improving the capacity of the ISO simulation remains a great challenge for future development of climate system models.

KEY WORDS IPCC AR5; intra-seasonal oscillation; Asian summer monsoon

Received 15 June 2016; Revised 6 December 2016; Accepted 9 January 2017

1. Introduction

The Asian summer monsoon is one of the major wind systems that changes with the seasons at the global scale. It includes three major components: the Indian monsoon (ISM), the East Asian monsoon (EASM) and the Western North Pacific monsoon (WNPSM). Previous studies showed that the intra-seasonal oscillation (ISO) in these regions critically influences the onset and break of Asian summer monsoon (Yasunari, 1979, 1980; Krishnamurti and Subrahmanyam, 1982; Chen and Chen, 1995; Wu, 2010), modulates the formation and frequency of tropical cyclones (Liebmann *et al.*, 1994; Maloney and Hartmann, 2000; Huang *et al.*, 2011), affects the occurrence of drought and flood events in the monsoon regions (Zhu *et al.*, 2003; Ju and Zhao, 2005). The extreme drought and precipitation events will definitely cause huge economic and human loss in the East and South Asia.

Evaluation and analysis of the monsoon ISO simulation in state-of-the-art models can provide us a clue to improve the capacity of seasonal forecast in the monsoon regions. Although the simulation of monsoon ISO has improved with the development of general circulation models (GCMs), there are still insufficiencies in ISO simulations due to the inadequate understanding of ISO mechanisms and impacts (Wang and Rui, 1990; Sperber *et al.*, 2001; Waliser *et al.*, 2003; Lin *et al.*, 2008; Sabeerali *et al.*, 2013). Waliser *et al.* (2003) evaluated the space–time variations of rainfall ISO and its teleconnection patterns simulated in atmospheric GCMs (AGCMs) and found that ISO patterns with somewhat northward propagation could be reproduced by most models, but lack sufficient eastward propagation. Lin *et al.* (2008) evaluated the sub-seasonal variabilities associated with the Asian summer monsoon in coupled models, which were prepared for the Intergovernmental Panel on Climate Change (IPCC) Fourth Assessment Report (AR4) and results showed the dominant spectral periods of 24–70-day and 12–24-day could be captured by only 4–5 models. Sabeerali *et al.* (2013) evaluated the boreal summer ISO simulated in the coupled

* Correspondence to: W. Hu, State Key Laboratory of Numerical Modeling for Atmospheric Sciences and Geophysical Fluid Dynamics (LASG), Institute of Atmospheric Physics, Chinese Academy of Sciences, P.O. Box 9804, Beijing 100029, China. E-mail: hwt@lasg.iap.ac.cn

models that participated in IPCC AR5 and determined that the boreal summer ISO cannot be properly simulated by these models.

As presented by previous studies, the capacity of ISO simulations could be influenced by varying horizontal/vertical resolution (Silvio *et al.*, 1996; Inness *et al.*, 2001), employing different cumulus parameterization schemes (Maloney and Hartmann, 2001; Grabowski, 2003; Randall *et al.*, 2003; Hu *et al.*, 2011) and taking air–sea interactions into account (Kemball-Cook and Wang, 2001; Fu *et al.*, 2002; Fu and Wang, 2004; Hu *et al.*, 2015). Therefore, it is of interest to assess the simulation capacity of the monsoon ISO and further examine the possible impact factors among the models. Building upon the study of Sabeerali *et al.* (2013), the current study also provides a comparison of background circulations, atmospheric internal dynamics and ocean–atmosphere interactions, which contribute to the ISO propagations, and discusses the possible impact of model resolution on the ISO simulation. The models, validation data and methodology are described in Section 2. Evaluation results are shown in Section 3. A summary and discussion is given in the last section.

2. Models, validation data and methodology

2.1. Models and validation data

Three historical ensembles of 9-year (1997–2005) daily mean model output derived from each IPCC AR5 coupled model are averaged and used for this analysis. The 19 models used here are BCC-CSM1.1, BNU-ESM, CanCM4, CanESM2, CCSM4, CNRM-CM5, CSIRO-MK3-6-0, EC-EARTH, FGOALS-g2, FGOALS-s2, GFDL-CM3, HadCM3, HadGEM2-CC, IPSL-CM5A-LR, MIROC4h, MIROC-ESM-CHEM, MPI-ESM-LR, MRI-CGCM3 and NorESM1-M. Table 1 shows the model names, the modelling groups, their horizontal and vertical resolutions and brief descriptions of their deep convection schemes.

The validation data sets include (1) GPCP (Global Precipitation Climatology Project; Huffman *et al.*, 2001) V2 daily precipitation data with a horizontal resolution of $1^\circ \times 1^\circ$; (2) ERA (ECMWF reanalysis)-interim data with a horizontal resolution of $1.5^\circ \times 1.5^\circ$ (Dee *et al.*, 2011). Several variables including horizontal winds, vertical velocity and surface specific humidity in ERA-interim reanalysis are used to examine the model simulation capacity in this study; (3) NOAA optimum interpolation (OI) SST V2 (Reynolds *et al.*, 2002) daily data ($1^\circ \times 1^\circ$). For consistency, all the variables in simulations and data sets used in this study are interpolated to the same spatial resolution ($2.5^\circ \times 2.5^\circ$), which cover nine summer seasons from May to October in the period of 1997–2005.

2.2. Methodology

Mean power spectrum (Gilman *et al.*, 1963) is used to obtain the common periodicity by taking the average of the individual power spectra for the nine summer seasons (May–October) in the period of 1997–2005. To isolate the intra-seasonal signal, the daily climatology is removed and Lanczos bandpass filter (Duchon, 1979) is applied, which will hereafter be referred to simply as 'filtered data'.

The ISO over Asian summer monsoon regions will be decomposed into three components in this study: An eastward-propagating component and a northward-propagating component in a period range of 30–80 days, with a 12–24-day westward-propagating ISO mode. The eastward component of the monsoon ISO may be extracted using the following method (Lin *et al.*, 2008). First, the 9-year ensemble-mean and interpolated daily precipitation data are averaged along the latitudes between 5° and 25°N. Then, we use the discrete Fourier transform and the inverse space–time Fourier transform to obtain the eastward component within 1–6 wavenumbers. Finally, through a 30–80-day Lanczos filter, the resultant eastward component with wavenumbers 1–6 is obtained (hereafter called the eastward component of the monsoon ISO). The westward counterpart (wavenumbers 1–6, 30–80-day precipitation anomaly) is isolated using the same method as above. The methods for the 12–24-day westward-propagating ISO mode and its eastward counterpart are similar, except that the precipitation data are averaged between 10° and 20°N and the filtered period is 12–24 days.

The lead–lag correlation technique is used to evaluate the propagation characteristics of precipitation associated with the ISO and the air–sea relationship area-averaged over the Indian Ocean and the Bay of Bengal (BOB). To examine northward and eastward features separately, the base point for calculation is chosen at 12.5°N, 85°E (for northward) and 15°N, 95°E (for eastward). For westward propagation, the reference point is 10°N, 120°E. Student's *t*-test is used to determine whether the correlation is significant.

3. Results

3.1. Simulations

3.1.1. Mean state and ISO variance

On the one hand, observational studies indicated that climatological convective intensity has a close relationship with the sub-seasonal variance of convection (Wheeler and Kiladis, 1999). On the other hand, some studies have shown the model biases of the ISO are related to the embedding mean field (e.g. Slingo *et al.*, 1996; Zhang *et al.*, 2006; Ajayamohan and Goswami, 2007). Therefore, we first evaluate the horizontal distributions of seasonal mean precipitation in boreal summer (May–October) over the monsoon regions (Figure 1). In the observations (Figure 1(a)), a large area of rainfall is located over the equatorial eastern Indian Ocean, the eastern BOB, the Indo-China Peninsula and the Western North Pacific (WNP). Sixteen of the coupled models can simulate the peak in the BOB region (BCC-CSM1.1, BNU-ESM, CanESM2, CCSM4, CNRM-CM5, CSIRO-MK3-6-0, FGOALS-g2, FGOALS_s2, GFDL-

Table 1. List of models used in this study including modelling group, model resolution and convection scheme details

Model name	Modelling groups	Resolution	Deep convection scheme/closure
BCC-CSM1.1	Beijing Climate Center (BCC), China Meteorological Administration, China	2.8125° × 2.8125° L26	Zhang and McFarlane (1995)/CAPE
BNU-ESM	GCESS, BNU, Beijing, China	2.8125° × 2.8125° L26	Zhang and McFarlane (1995)/CAPE
CanCM4	Canadian Centre for Climate Modelling and Analysis, Canada	2.8125° × 2.7673° L35	Zhang and McFarlane (1995)/CAPE
CanESM2			
CCSM4	National Center for Atmospheric Research, United States	0.9° × 1.25° L26	Zhang and McFarlane (1995)/CAPE
CNRM-CM5	Centre National de Recherches Météorologiques, France	1.40625° × 1.40625° L31	Bougeault (1985)/Kuo-type
CSIRO-MK3-6-0	Commonwealth Scientific and Industrial Research Organization, Australia	1.875° × 1.875° L18	Gregory *et al.* (1997)/cloud-base buoyancy
EC-EARTH	EC-EARTH consortium, ECMWF	1.125° × 1.125° L62	Fritsch and Chappell (1980); Nordeng (1994)/CAPE
FGOALS-g2	LASG, Institute of Atmospheric Physics, Chinese Academy of Sciences and CESS, Tsinghua University, China	3° × 2.8125° L26	Zhang and Mu (2005)/CAPE change
FGOALS-s2	LASG, Institute of Atmospheric Physics, Chinese Academy of Sciences, China	1.6667° × 2.8125° L26	Tiedtke (1989); Nordeng (1994)/CAPE
GFDL-CM3	NOAA Geophysical Fluid Dynamics Laboratory, United States	2° × 2.5° L48	Moorthi and Suarez (1992)/CAPE
HadCM3	Met Office Hadley Centre, UK	2.4658° × 3.75° L19	Gregory *et al.* (1997)/cloud-base buoyancy
HadGEM2-CC	Met Office Hadley Centre, UK	1.2414° × 1.875° L60	Derbyshire *et al.* (2011)/adaptive detrainment
IPSL-CM5A-LR	Institut Pierre Simon Laplace, Paris, France	1.875° × 3.75° L39	Emanuel (1991)/episodic mixing and buoyancy sorting
MIROC4h	Atmosphere and Ocean Research Institute (The University of Tokyo), National Institute for Environmental Studies and Japan Agency for Marine-Earth Science and Technology, Japan	0.5625° × 0.5625° L56	Pan and Randall (1998), Chikira and Sugiyama (2010)/CAPE
MIROC-ESM-CHEM	Japan Agency for Marine-Earth Science and Technology, Atmosphere and Ocean Research Institute (The University of Tokyo) and National Institute for Environmental Studies, Japan	2.8125° × 2.8125° L80	Arakawa and Schubert (1974), Emori *et al.* (2001)/CAPE
MPI-ESM-LR	Max Planck Institute for Meteorology, Germany	1.875° × 1.875° L47	Tiedtke (1989); Nordeng (1994)/CAPE
MRI-CGCM3	Meteorological Research Institute, Japan	1.125° × 1.125° L48	Tiedtke (1989)/CAPE
NorESM1-M	Norwegian Climate Centre, Norway	1.875° × 2.5° L26	Zhang and McFarlane (1995)/CAPE

CM3, HadCM3, HadGEM2-CC, IPSL-CM5A-LR, MIROC4h, MIROC-ESM-CHEM, MPI-ESM-LR and NorESM1-M). However, most of the models underestimate the precipitation intensity over the BOB and WNPSM region, while six models (CSIRO-MK3-6-0, FGOALS-g2, HadCM3, HadGEM2-CC, MIROC4h and MPI-ESM-LR) overestimate the rainfall amount. This is consistent with the result of Sabeerali *et al.* (2013), which showed that almost all models cannot reproduce the exact precipitation intensities over the ASM regions. Furthermore, in the current study, nearly all the models (except for HadCM3, HadGEM2-CC and MIROC4h) fail to reproduce the northeast–southwest-tilted rain belt in the EASM region.

Figure 2 shows the standard deviation (shading) of 12–90-day filtered precipitation anomaly and its percent variance (contour) accounting for raw precipitation anomaly for both observations and models. The maxima of standard deviation in observations are located over the eastern Arabian Sea, BOB and the South China Sea (SCS).

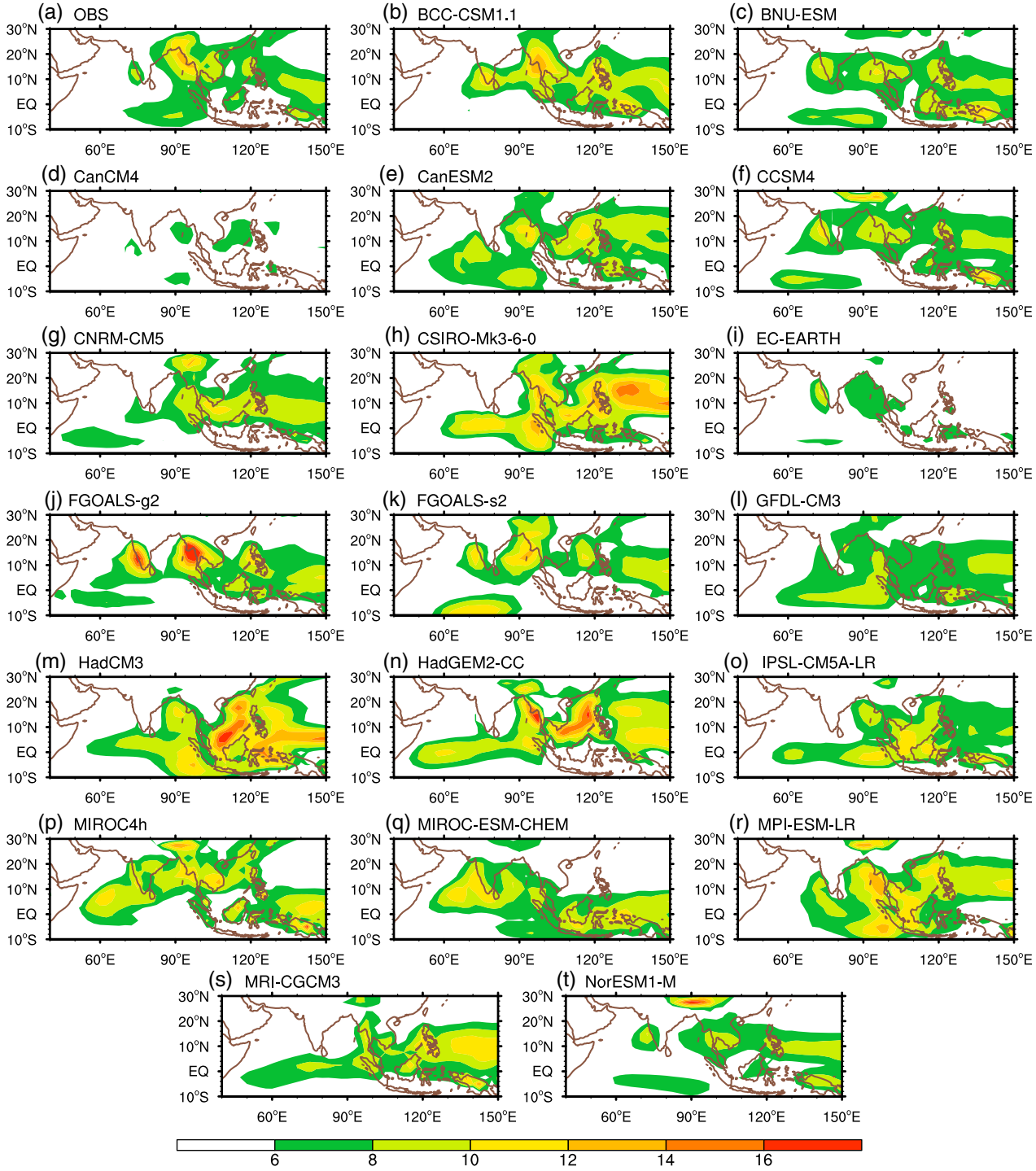

Figure 1. Seasonal mean precipitation (mm day^{-1}) in boreal summer (May–October) for (a) the GPCP and (b)–(t) the 19 coupled models in the period of 1997–2005.

With the exception of BCC-CSM1.1, FGOALS-g2 and HadGEM2-CC, which simulate a larger magnitude of variability, the other 16 models all somewhat underestimate the peak value. Three coupled models (BNU-ESM, CCSM4 and MIROC4h) could reasonably reproduce near-realistic magnitude and horizontal patterns of standard deviation. Percent variance of 12–90-day precipitation anomaly accounting for raw anomaly is larger than 30% in the Arabian Sea, BOB, equatorial Indian Ocean and SCS. The area with large percent variance is in good agreement with the region with large standard deviation (Figure 2(a)). A total of 16 of 19 models (except for CCSM4, CNRM-CM5 and MIROC4h) have larger percent variance than 40% in the North Indian Ocean (NIO) or SCS or WNP.

To better compare the intensity of variance of precipitation anomaly among the models, the magnitudes of intra-seasonal (12–90-day) variance generated by averaging the longitudes of 60°–100°E and 120°–160°E and the latitudes of 5°–25°N are shown in Figure 3. In observations (Figure 3(a)), two peaks of variance

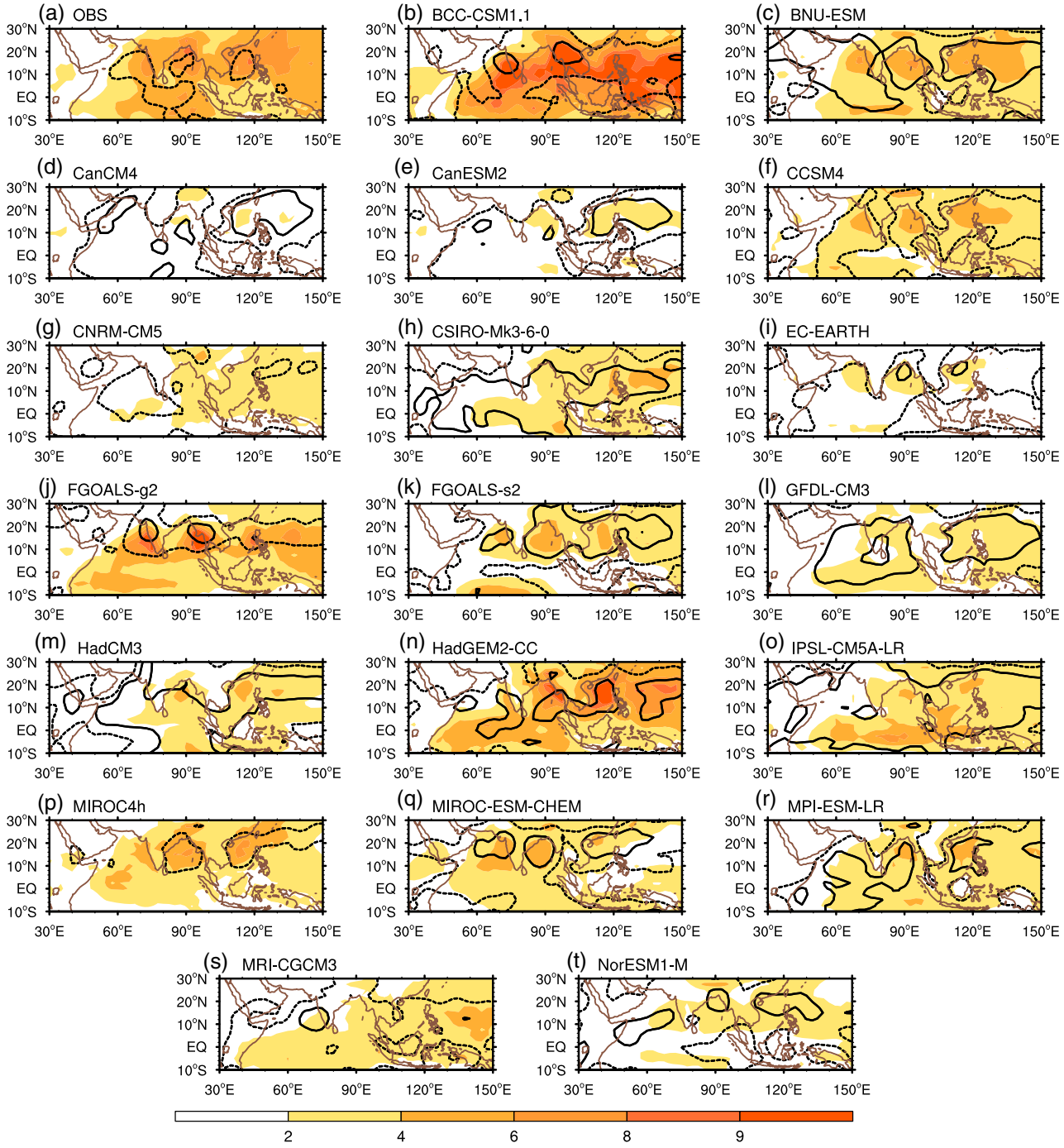

Figure 2. Standard deviation (shading) of 12–90-day filtered precipitation anomaly and its percent variance accounting for raw precipitation anomaly (contour, %) during boreal summer (May–October) for (a) observations and (b)–(t) 19 coupled models in the period of 1997–2005. Black dashed contours represent percent variance of 30% and black solid contours represent 40%.

appear in two latitudes (15° and 5°S). The sub-seasonal variance in most of the models is smaller than that in observations; however, two models (BCC-CSM1.1 and FGOALS_g2) simulate a much stronger variance in the Northern Hemisphere. Previous studies showed that the model biases in ISO variance mostly come from inaccurate simulations of the seasonal mean precipitation (Sperber and Annamalai, 2008; Sabeerali *et al.*, 2013). Thus, the stronger variance presented in BCC-CSM1.1 and FGOALS_g2 are possibly due to the overly large seasonal mean precipitation. Figure 3(b) shows the total sub-seasonal variance in the WNP region, which has only one peak in the 10°–20°N latitudinal zone. Two models (BCC-CSM1.1 and HadGEM2-CC) produce larger amplitude of ISO variance, while the ISO variance simulated by BCC-CSM1.1 presents another incorrect peak in the Southern Hemisphere, of which the magnitude is three times larger than observed. Apart from the above models, the other models all underestimate the variance.

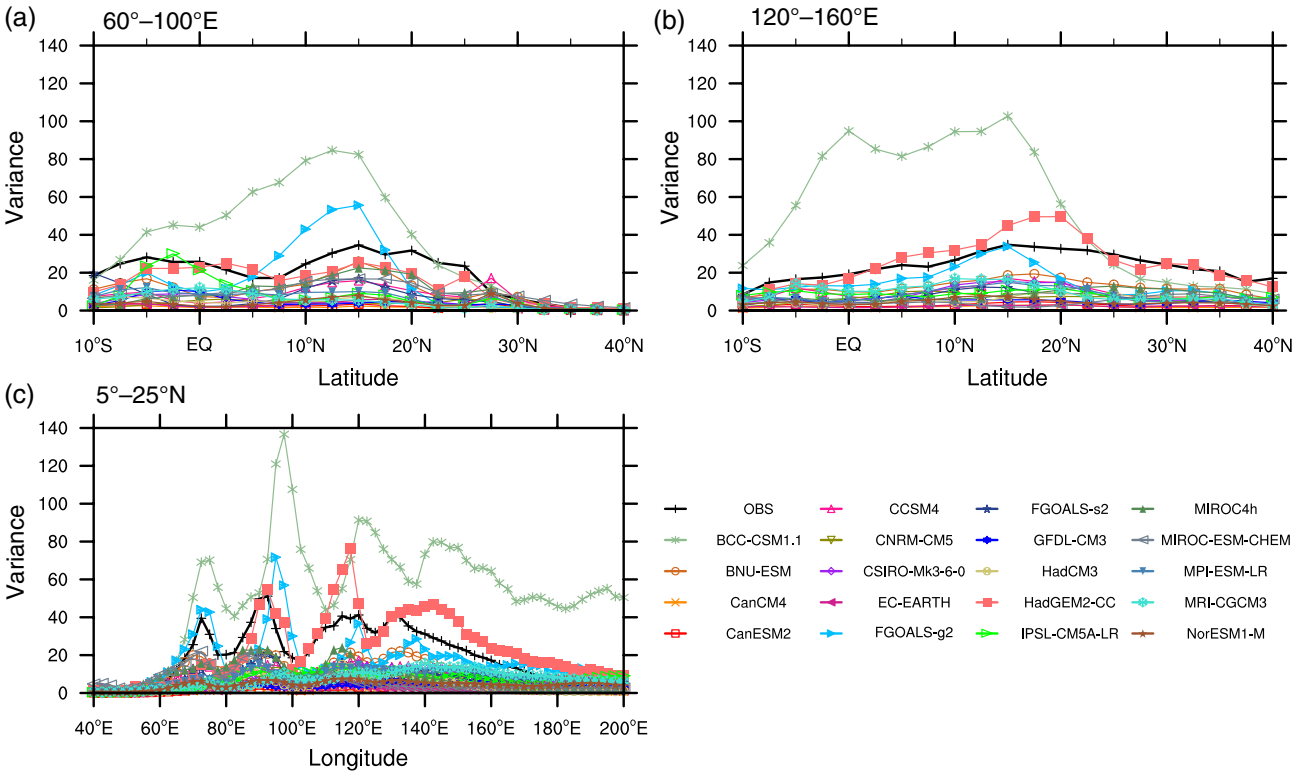

Figure 3. Meridional profile of the intra-seasonal (12–90-day) variance of precipitation anomaly averaged (a) between 60° and 100°E and (b) between 120° and 160°E and (c) zonal profile averaged between 5° and 25°N for observations and 19 IPCC AR5 coupled models during boreal summer (May–October) in the period of 1997–2005. Units: $(\text{mm day}^{-1})^2$.

The variance along the longitudes shown by the observations displays three peaks, respectively, located at the Arabian Sea, the BOB and SCS plus WNP (Figure 3(c)). The variance magnitude simulated by BCC-CSM1.1 is stronger than the observations in a vast longitude band of 60°–200°E. Moreover, FGOALS_g2 (HadGEM2-CC) shows larger variance in the BOB (SCS and WNP). The monsoon variability simulated by other coupled models shows similar pattern but a smaller variance value. Many of the models cannot reproduce sufficient rainfall over some specific regions (Figure 1). Note that simulating realistic seasonal mean precipitation is a necessary but not sufficient condition for the simulation of ISO (Sperber and Annamalai, 2008). The simulation capacity of ISO by models does not completely depend on the correct simulation of seasonal mean. Thus, it is also important to examine ISO simulation in other ways.

3.1.2. *Dominant periodicity*

The ISO of the Asian summer monsoon can be described by two dominant modes. One is a low-frequency eastward- and northward-propagating boreal summer ISO, which has been analysed in depth by many meteorologists (e.g. Kemball-Cook and Wang, 2001; Hsu and Weng, 2001; Lawrence and Webster, 2002; Straub and Kiladis, 2003; Jiang *et al.*, 2004). The second mode is westward-propagating with a quasi-biweekly period (e.g. Krishnamurti and Ardunay, 1980; Murakami, 1980; Lau and Lau, 1990; Hartmann *et al.*, 1992; Kiladis and Weickmann, 1997; Chen *et al.*, 2000; Mao and Chan, 2005). It is necessary to evaluate the dominant periodicity over the Asian summer monsoon region at first. Therefore, the power spectral analysis is used to compare the dominant periodicity of precipitation anomaly simulated by the models with the observation in the regions of 5°–25°N, 60°–100°E (NIO; Figure 4) and 10°–20°N, 120°–170°E (WNP; Figure 5). Upper confidence bound for Markov (black dotted lines) is used to examine the significance of 95% confidence level.

For the 9-summer average, Figure 4 shows the power spectra of the unfiltered precipitation anomalies area-averaged over the NIO. It is apparent that there is a spectral peak in the day of 40 reach 95% confidence level in the observation (Figure 4(a)). There are two significant spectral peaks within low-frequency and quasi-biweekly periods in the simulations of five models (BNU-ESM, GFDL-CM3, MIROC-ESM-CHEM, MRI-CGCM3 and NorESM1-M). There is a significant peak within the period of smaller than 30 days in 11 models (BCC-CSM1.1, CCSM4, CNRM-CM5, CSIRO-MK3-6-0, EC-EARTH, FGOALS-s2, HadCM3, HadGEM2-CC, IPSL-CM5A-LR, MIROC4h and MPI-ESM-LR). However, the spectral peak in three models (CanCM4, CanESM2 and FGOALS-g2) does not pass the 95% confidence level.

As for the region of WNP, the observation shows that the spectral peak occurs at approximately 20-day (Figure 5(a)). Ten models (BCC-CSM1.1,

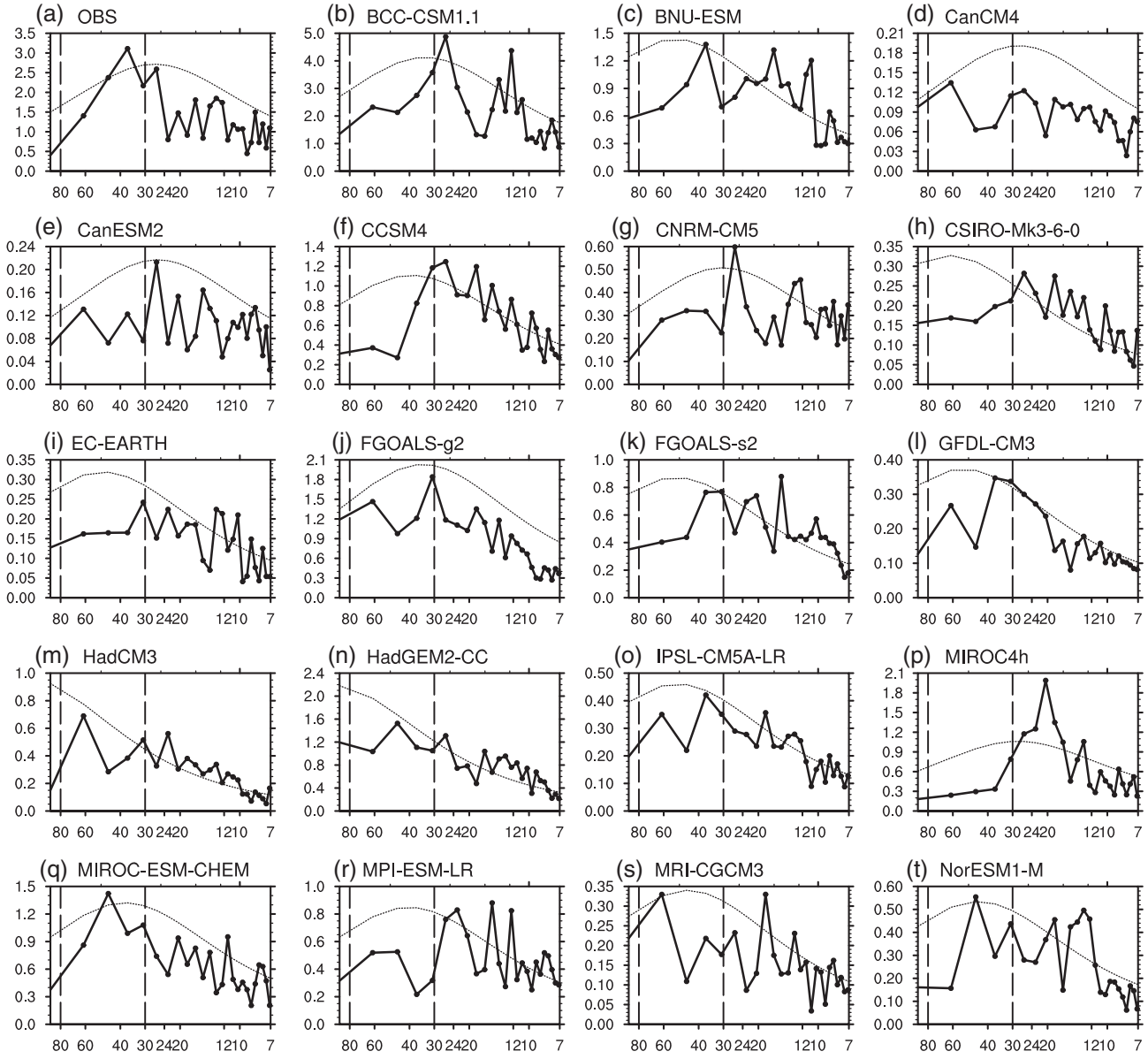

Figure 4. The averaged power spectra of the unfiltered precipitation area-averaged over the NIO (5°–25°N, 60°–100°E) for (a) GPCP and (b)–(t) 19 coupled models during boreal summer (May–October) in the period of 1997–2005. The black dotted lines represent a 95% confidence level.

CNRM-CM5, CSIRO-MK3-6-0, EC-EARTH, HadCM3, HadGEM2-CC, MIROC4h, MPI-ESM-LR, MRI-CGCM3 and NorESM1-M) could simulate the peak within the quasi-biweekly period similar to the observed. The significant spectral peak in four models (BNU-CSM, CCSM4, FGOALS-s2 and GFDL-CM3) occurs around 30-day. However, three models (FGOALS-g2, IPSL-CM5A-LR and MIROC-ESM-CHEM) simulate the dominant periods larger than 30 days. The spectral peaks in two models (CanCM4 and CanESM2) are not significant.

3.1.3. Propagation characteristics

The point-based lead–lag correlation technique is used to demonstrate more detailed characteristics of ISO propagation. The meridional propagations of the 30–80-day precipitation anomaly averaged between 70°–100°E with respect to itself at 12.5°N, 85°E can be seen in Figure 6. Observations in ISO propagation show the obvious northward movement from equator to farther north and southward movement in the Southern Hemisphere. A total of 10 of the 19 models (BCC-CSM1.1, BNU-ESM, CCSM4, CNRM-CM5, EC-EARTH, FGOALS_s2, HadCM3, MIROC4h, MIROC-ESM-CHEM and MRI-CGCM3) could briefly reproduce the northward propagation. Moreover, compared with the consistently good performance in simulating the northward propagation in the Northern Hemisphere, southward-moving signals in the Southern Hemisphere seem to be difficult to reproduce for many models except two models (MIROC-ESM-CHEM and MRI-CGCM3).

In addition to the clear northward movement of convection systems over the Asian monsoon regions in boreal summer, another feature of 30–80 day ISO mode is presented as ISO signals propagating eastward

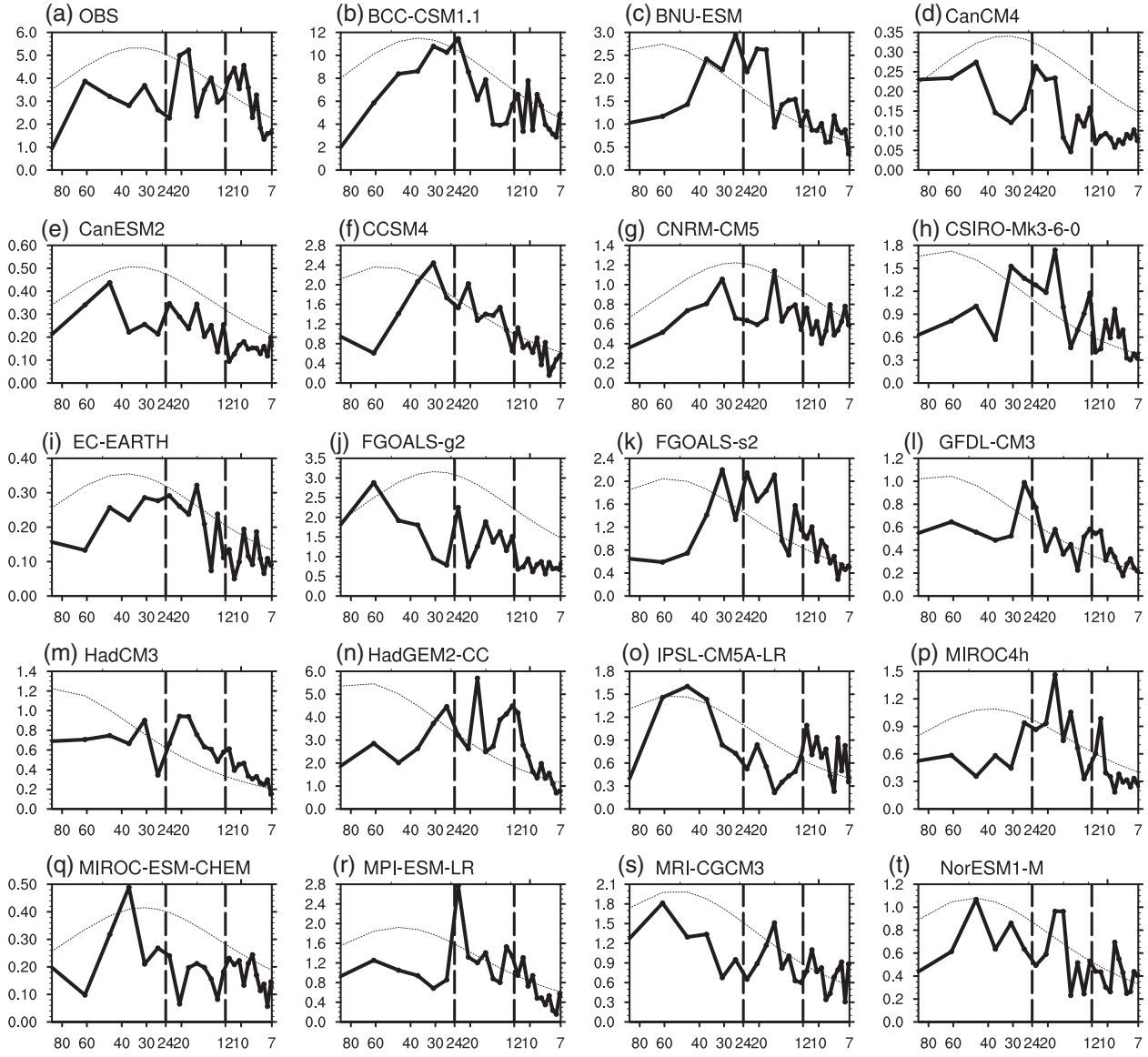

Figure 5. The averaged power spectra of the unfiltered precipitation area-averaged over the WNP (10°–20°N, 120°–170°E) for (a) GPCP and (b)–(t) 19 coupled models during boreal summer (May–October) in the period of 1997–2005. The black dotted lines represent a 95% confidence level.

in the off-equatorial regions. The zonal propagation features of tropical ISO averaged from 5° to 25°N are shown in Figure 7. Results show that only two models (GFDL_CM3 and IPSL-CM5A-LR) can reproduce the realistic propagation eastward from 40° to 120°E and westward in WNP region similar to the observations. Other models still have difficulties in simulating a reasonable propagation along the off-equatorial latitudes. Among these models, differences in biases of propagation characteristics are existed. Eleven models (BCC-CSM1.1, CanCM4, CanESM2, CNRM-CM5, CSIRO-MK3-6-0, FGOALS-g2, HadCM3, HadGEM2-CC, MIROC4h, MPI-ESM-LR and MRI-CGCM3) present nearly stationary convection anomalies in the NIO. Nevertheless, six models (BNU-ESM, CCSM4, EC-EARTH, FGOALS-s2, MIROC-ESM-CHEM and NorESM1-M) show obvious westward propagation of convection anomalies in the NIO, SCS and WNP.

Figure 8 compares the characteristics in westward propagations of the 12–24-day ISO mode averaged between 10° and 20°N simulated in the models with the observed. In the observations, there is an obvious westward propagation from 130° to 110°E (Figure 8(a)). A total of 12 of 19 models (BNU-CSM, CanCM4, CanESM2, CCSM4, CNRM-CM5, EC-EARTH, FGOALS-s2, HadCM3, MIROC4h, MIROC-ESM-CHEM, MPI-ESM-LR and NorESM1-M) could briefly capture the westward-propagation feature in the WNP similar to the observed. However, three models (CSIRO-MK3-6-0, GFDL-CM3 and IPSL-CM5A-LR) present nearly stationary or eastward propagation around 120°E. Three models (BCC-CSM1.1, FGOALS-g2 and MRI-CGCM3) only show the westward propagation to the west of 120°E.

In the following parts, we discuss the simulation capabilities according to three aspects: low-frequency northward

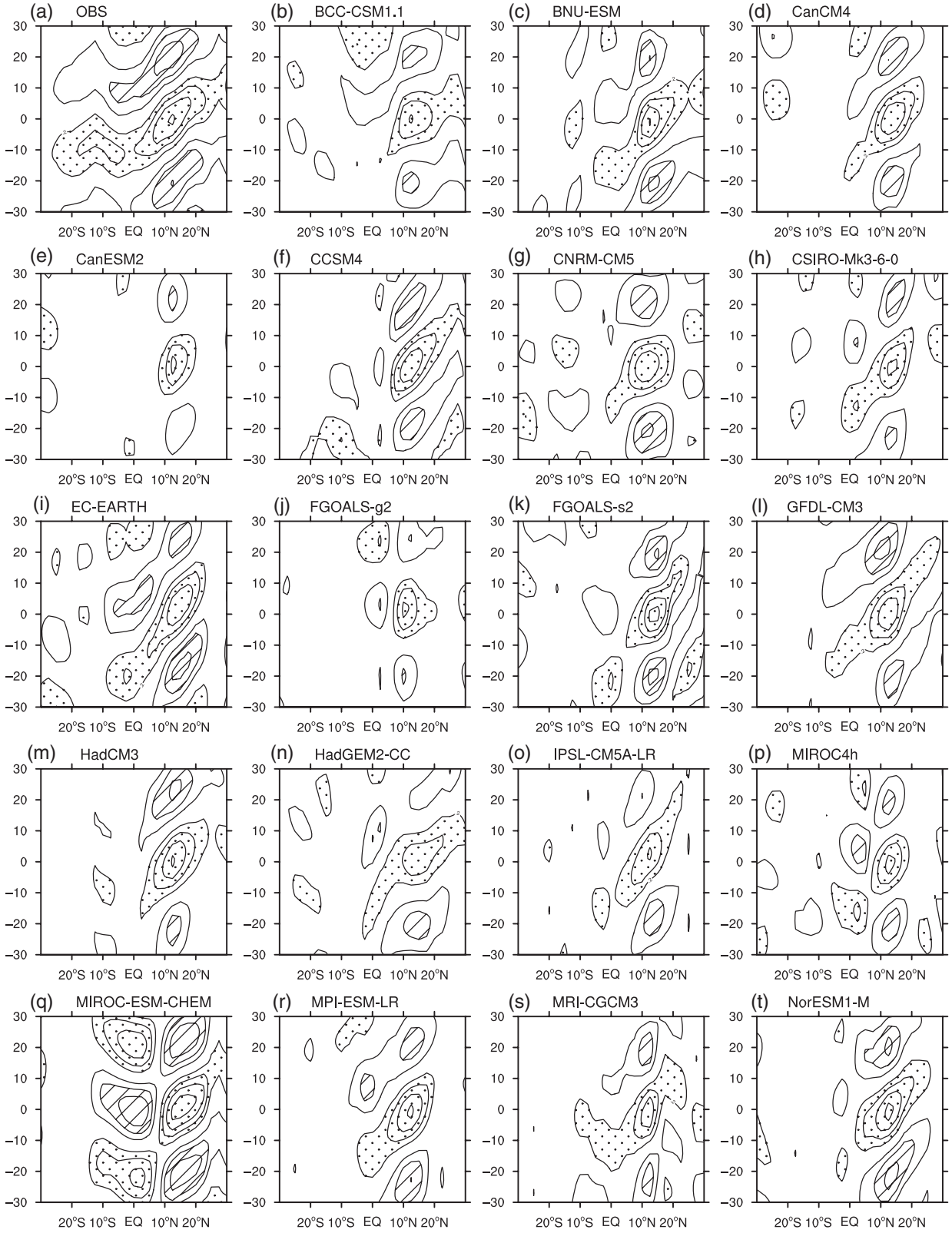

Figure 6. Meridional propagations of the 30–80-day ISO mode along the longitudes between 70° and 100°E for (a) observations and (b)–(t) 19 IPCC AR5 coupled models during boreal summer (May–October) in the period of 1997–2005 derived from GPCP and model precipitation. The calculation method is point-based lead–lag correlation analysis with reference to the point at 12.5°N, 85°E. The gridded areas are the regions above 95% in the significance tests.

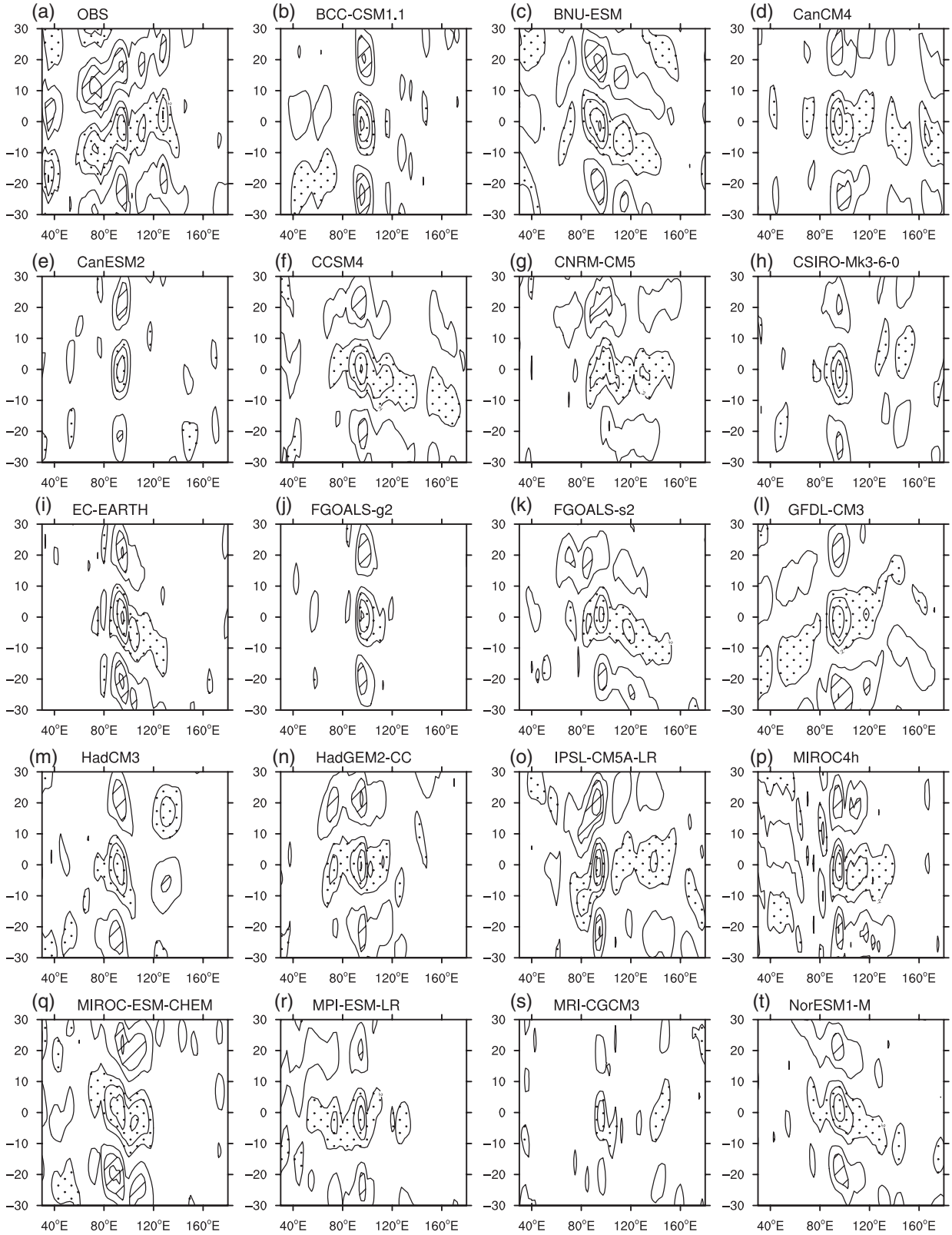

Figure 7. Zonal propagations of the 30–80-day ISO mode along the latitudes between 5° and 25°N for (a) observations and (b)–(t) 19 IPCC AR5 coupled models during boreal summer (May–October) in the period of 1997–2005 derived from GPCP and model precipitation. The calculation method is point-based lead–lag correlation analysis with reference to the point at 15°N, 95°E. The gridded areas are the regions above 95% in the significance tests.

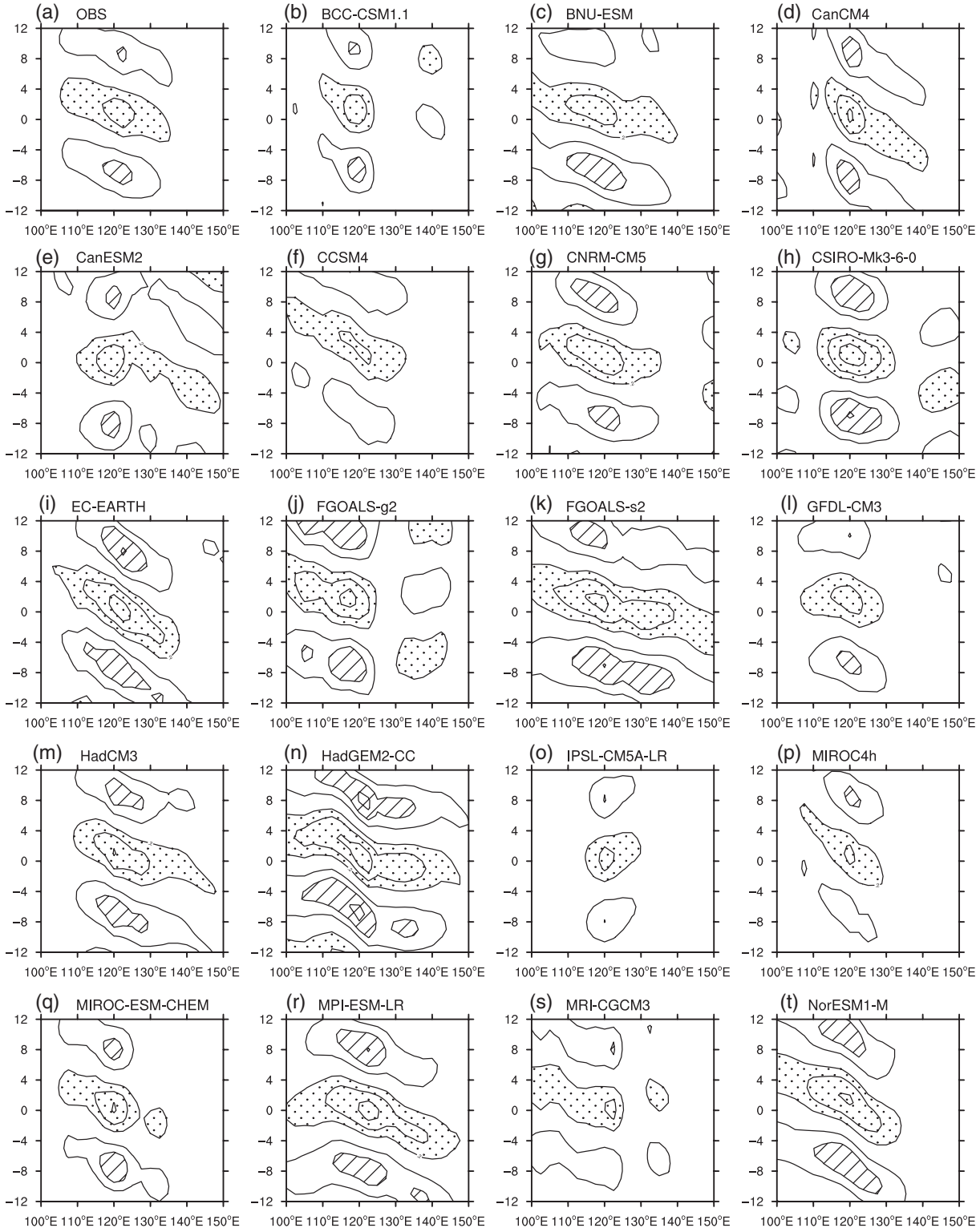

Figure 8. Zonal propagations of the 12–24-day ISO mode along the latitudes between 10° and 20°N for (a) observations and (b)–(t) 19 IPCC AR5 coupled models during boreal summer (May–October) in the period of 1997–2005 derived from GPCP and model precipitation. The calculation method is point-based lead–lag correlation analysis with reference to the point at 10°N, 120°E. The gridded areas are the regions above 95% in the significance tests.

propagation, low-frequency eastward propagation and high-frequency westward propagation. First, the variance of ISO eastward component is analysed, removing the variance contribution of westward component as introduced in Section 2. Figure 9(a) presents the variance of ISO eastward component (30–80 day) averaged between 5° and 25°N. Observations show that the peak of variance over the BOB reach to approximately 0.25 $(\text{mm day}^{-1})^2$ and all models except BCC-CSM1.1 underestimate the value. However, the maxima of variance simulated by

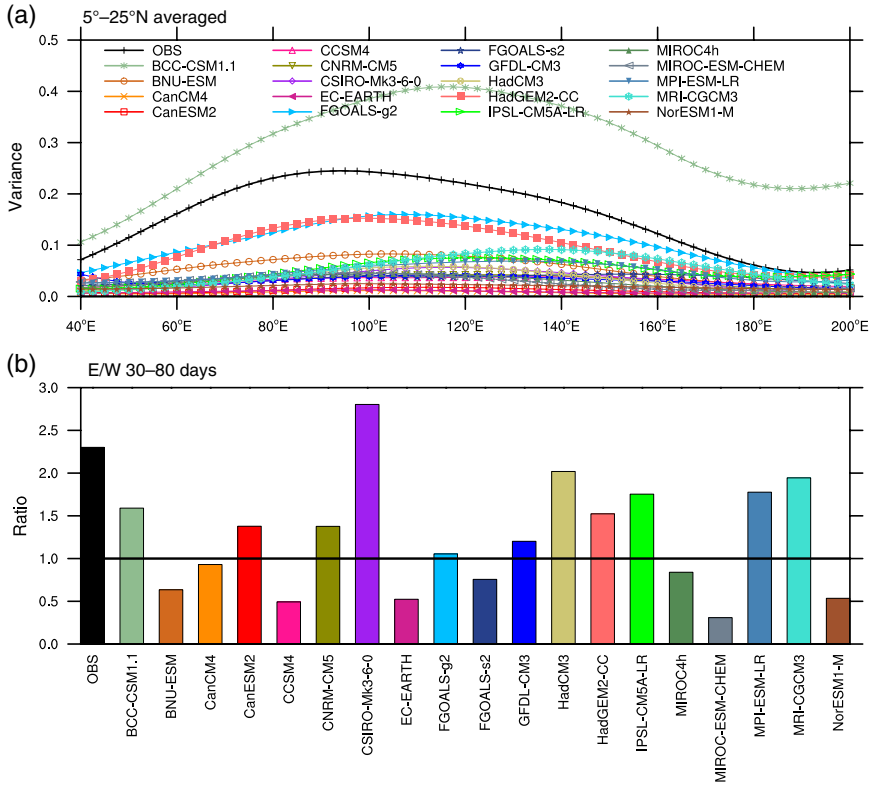

Figure 9. (a) Variance of the eastward-propagating 30–80-day ISO mode averaged between 5° and 25°N for the observations and 19 models during boreal summer (May–October) in the period of 1997–2005 derived from GPCP and model precipitation. Units: $(\text{mm day}^{-1})^2$; (b) ratio of the variance of the eastward mode and the variance of westward counterpart (both are 30–80-day mode) for observations and 19 models, area averaged over 5–25°N and 60–120°E.

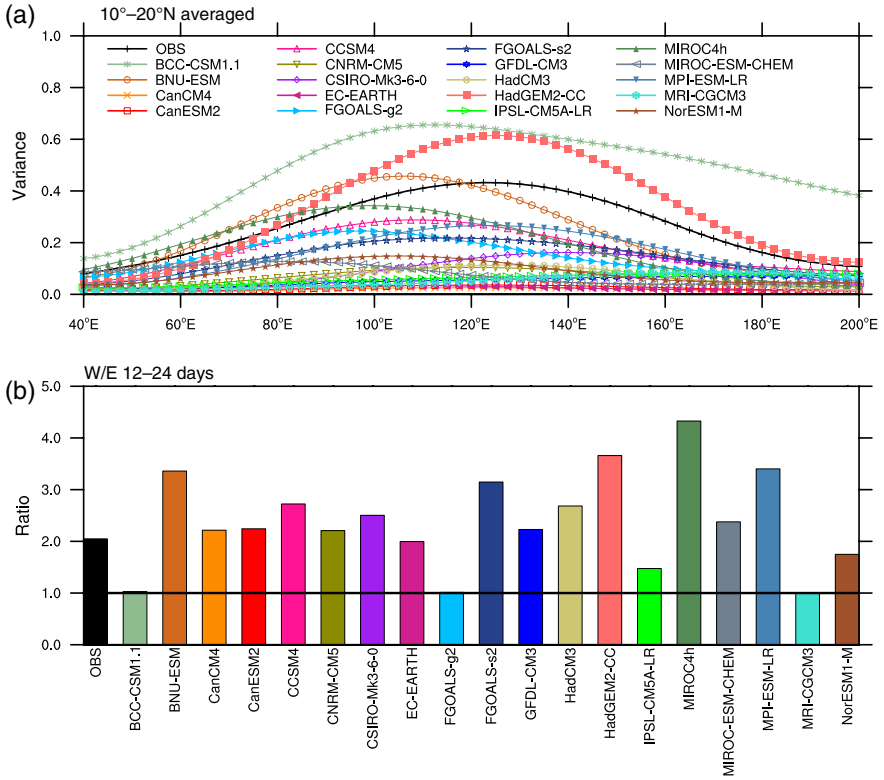

Figure 10. (a) Variance of the westward-propagating 12–24-day ISO mode averaged between 10° and 20°N for the observations and 19 models. Units: $(\text{mm day}^{-1})^2$; (b) ratio of the variance of the westward mode and the variance of eastward counterpart (both are 12–24-day mode) for observations and 19 models during boreal summer (May–October) in the period of 1997–2005 derived from GPCP and model precipitation, area averaged over 10–20°N and 120–170°E.

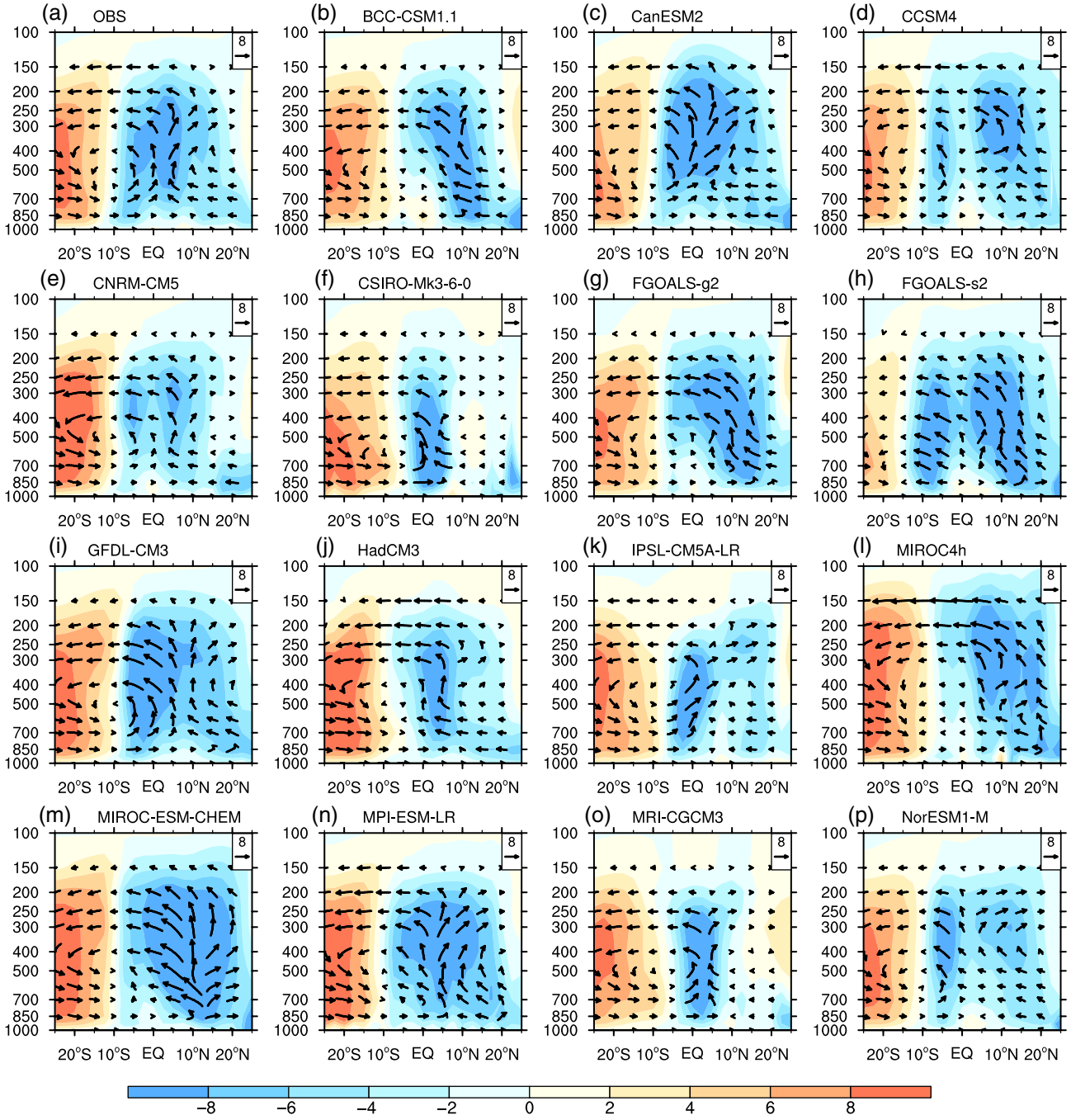

Figure 11. Seasonal (May–October) mean Hadley circulation averaged over 70°–90°E for (a) observations and (b–p) 15 coupled models in the period of 1997–2005 derived from ERA-interim reanalysis and model data. Vertical velocity (shading) is multiplied by the ratio of meridional wind divide vertical velocity. Units: omega (Pa s^{-1}); meridional wind (m s^{-1}).

nine models (BCC-CSM1.1, CCSM4, CSIRO-Mk3-6-0, EC-EARTH, FGOALS-g2, FGOALS-s2, HadCM3, IPSL-CM5A-LR and MRI-CGCM3) are located over the SCS or the WNP.

Furthermore, another important method for evaluating the eastward component is the ratio between the variance of the eastward-propagating ISO and that of its westward counterpart (westward wavenumber 1–6, 30–80-day mode), which was used by Lin *et al.* (2008) to evaluate the sub-seasonal variability associated with Asian summer monsoon simulated by IPCC AR4 coupled GCMs. Figure 9(b) shows the ratio area-averaged over 5°–25°N and 60°–120°E. Observational results display that the eastward variance is about 2.4 times the westward variance. Of the 19 models, ten models (BCC-CSM1.1, CanESM2, CNRM-CM5, CSIRO-MK3-6-0, GFDL-CM3, HadCM3, HadGEM2-CC, IPSL-CM5A-LR, MPI-ESM-LR and MRI-CGCM3) show that the eastward propagation is dominant and simulate a more realistic ratio than the other models.

We further evaluate the westward propagations of the 12–24-day ISO mode. Figure 10(a) shows the

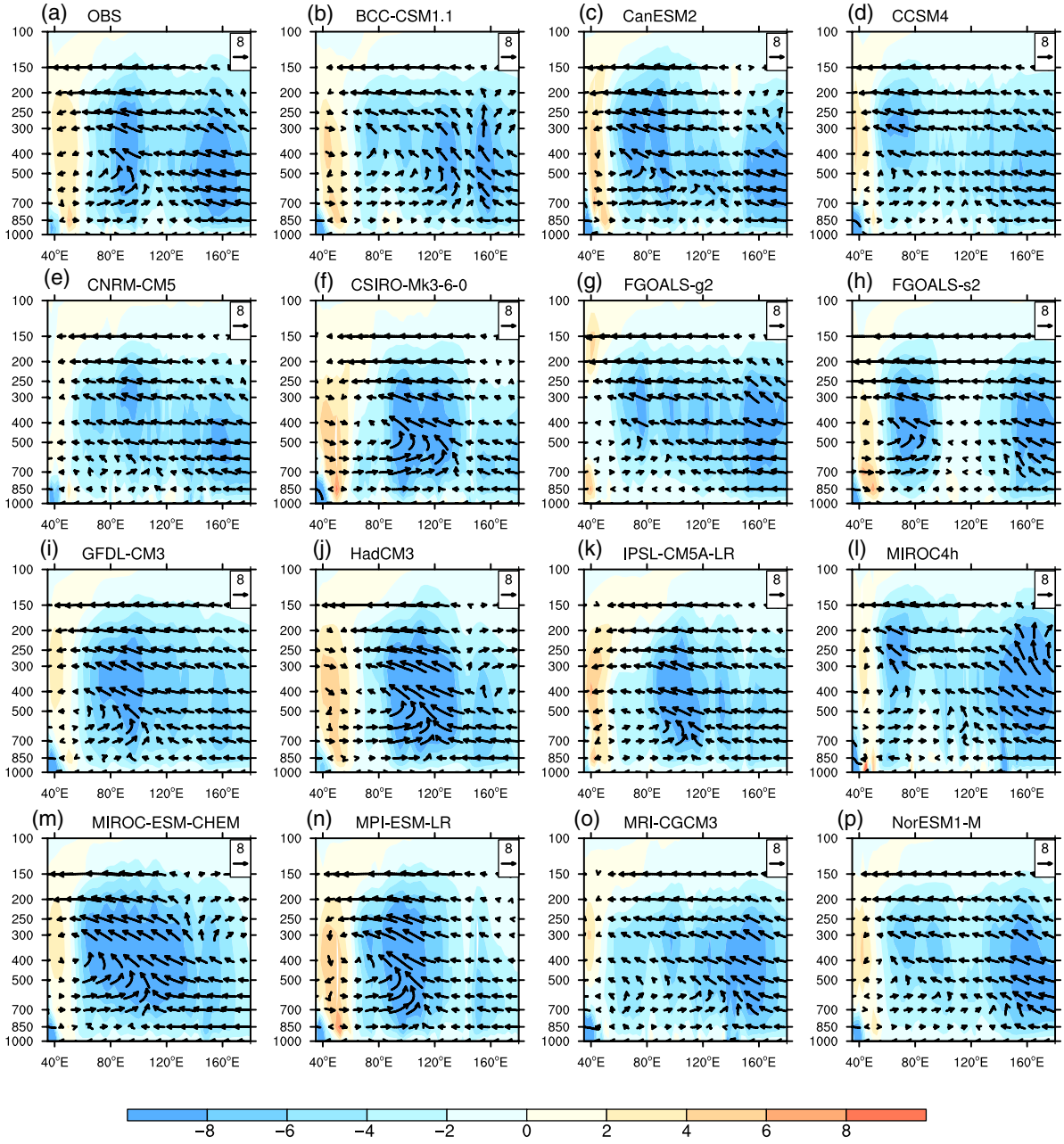

Figure 12. Seasonal (May–October) mean Walker circulation averaged over 10°S–10°N for (a) observations and (b–p) 15 coupled models in the period of 1997–2005 derived from ERA-interim reanalysis and model data. Here, vertical velocity (shading) is multiplied by the ratio of meridional wind divide vertical velocity. Units: omega (Pa s^{-1}); zonal wind (m s^{-1}).

10°–20°N averaged variance of the westward-propagating 12–24-day ISO mode. The maximum of the observed variance (up to 0.43 (mm day^{-1})^2) locates over the WNP. The variances in three models (BCC-CSM1.1, BNU-ESM and HadGEM2-CC) are larger and only the maximum of HadGEM2-CC is located in the WNP as observed. Moreover, other models present small variance values of westward-propagating ISO or indicate an incorrect maximum region (over Indian Ocean).

During the 12–24-day period, the ratio between the variance of the westward and eastward counterpart area averaged over 10°–20°N and 120°–170°E is determined (Figure 10(b)). In the observations, the westward component is approximately two times that of the eastward component. Almost all the models (except BCC-CSM1.1, FGOALS_g2 and MRI-CGCM3) simulate ratios larger than one, which indicates that the westward component is dominant, and indicates a substantially larger ratio than observed.

3.2. Evaluations of possible factors in ISO simulation

3.2.1. Hadley and Walker circulation

Sikka and Gadgil (1980) pointed out that the simulated ISO with a period similar to that of the observed is related to an interaction between organized convection and large-scale Hadley circulation. An unrealistic local Hadley or Walker circulation affects the simulation of vertical

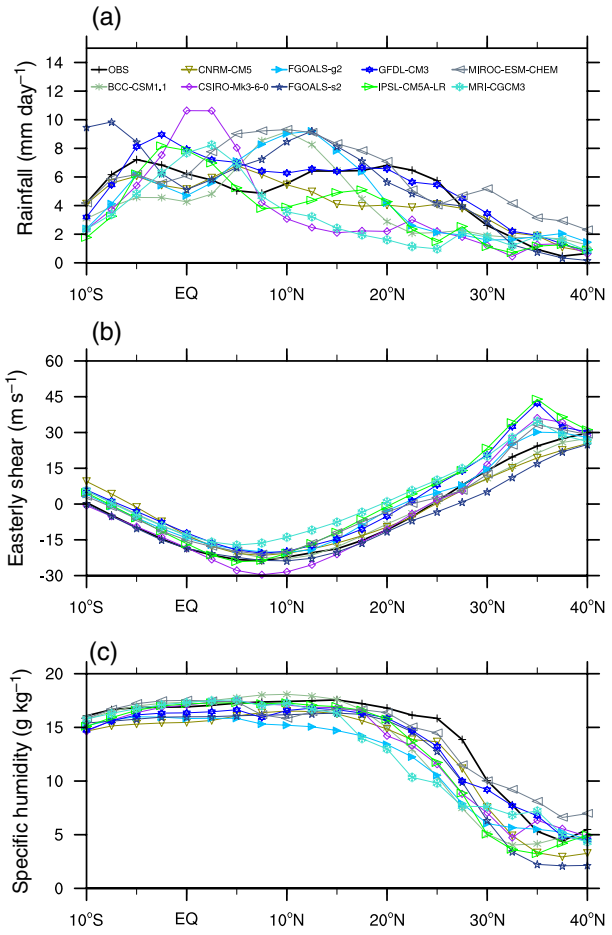

Figure 13. Seasonal (May–October) mean meridional distribution of (a) rainfall (mm day^{-1}; GPCP and model precipitation), vertical shear (u200–u850, m s^{-1}) and specific humidity (g kg^{-1}) at 1000 h Pa (ERA-interim reanalysis and model data) averaged over the longitudinal band 70°–90°E for nine model simulations compared with OBS (black solid curve) in the period of 1997–2005.

motion, which will cause model biases of intra-seasonal rainfall (Goswami, 2005; Wang *et al.*, 2006; Goswami *et al.*, 2014). Thus, further analysis in model biases of the seasonal mean Hadley or Walker circulation are still needed to evaluate. The simulated May–October regional Hadley circulation (Figure 11; averaged over 70°–90°E) and the Walker circulation (Figure 12; averaged over 10°S–10°N) for 15 coupled models are compared with the ERA-interim reanalysis. Figure 11(a) shows that there are two ascending branches over the Indian sub-continent and south of the equator in the ERA-interim reanalysis, while a strong subsidence exists further south to the equator (approximately to the south of 10°S). Nearly all the coupled models are able to simulate the descending branch in the Southern Hemisphere (Figures 11(b)–(p)). However, model biases are still existed, which can be summarized as follows: First, the excessive upward motions over the Indian sub-continent simulated by BCC-CSM1.1, CCSM4, FGOALS-g2, FGOALS-s2, MIROC4h, MIROC-ESM-CHEM and MPI-ESM-LR are in agreement with the precipitation pattern in Figure 1; second, the missing ascending branch over the latitude band 10°S–0° is simulated by BCC-CSM1.1, CSIRO-MK3-6-0, HadCM3, MIROC4h and MRI-CGCM3; third, some models (CSIRO-MK3-6-0, IPSL-CM5A-LR and MRI-CGCM3) simulate an inadequate ascending motion over the monsoon region. Goswami *et al.* (2014) showed that the local Hadley cell bias relates well with the model biases of moisture convergence, which will cause a local dry/wet bias in models. Thus, the model biases summarized above may result in the error of moisture convergence, which may be related to the migration of convection anomalies.

In addition, Figure 12a shows the maxima of upward motion of seasonal mean Walker circulation in the ERA-interim reanalysis are located over two longitude bands (80°–100°E and 140°–170°E). Almost all the models somewhat reproduce the ascending branch over the Great Warm Pool. However, six models (CanESM2, CCSM4, FGOALS-g2, FGOALS-s2, MIROC4h and MIROC-ESM-CHEM) exaggerate the upward motions to the west of 80°E along the latitude band of 10°S–10°N, which results in good agreement with the *in situ* overly large precipitation (Figures 12(c), (d), (g), (h), (l), (m) *.vs* Figures 1(e), (f), (j), (k), (p), (q)). The entire models underestimate the ascending motion which occurs near 160°E presented by the ERA-interim reanalysis. The evaluations of seasonal mean Hadley and Walker circulations provide a background statement that is connected to the precipitation biases and its intra-seasonal variability (Sikka and Gadgil, 1980; Goswami, 2005; Wang *et al.*, 2006; Goswami *et al.*, 2014). In the next section, we undertake more detailed evaluations with respect to atmospheric internal dynamics and air–sea interactions.

3.2.2. *Atmospheric internal dynamics*

Jiang *et al.* (2004) stated that the vertical easterly shear of the mean flow contributes to the northward shift of the convective heating. Figure 13 shows the meridional variation of the climatological rainfall (mm day^{-1}, Figure 13(a)), vertical easterly shear (m s^{-1}, Figure 13(b)) and specific humidity at 1000 h Pa (g kg^{-1}, Figure 13(c)) averaged over the longitudinal band of 70°–90°E for the model simulations compared with the GPCP and ERA-interim reanalysis. From results of GPCP, the two peaks of seasonal mean rainfall in boreal summer are located over the latitude bands 10°S–0° and to the north of 20°N. Most of the models simulate stronger precipitation near the equator but relatively little rainfall to the north of 20°N. It is evident that all of the nine models (BCC-CSM1.1, CNRM-CM5, CSIRO-MK3-6-0, FGOALS-g2, FGOALS-s2, GFDL_CM3, IPSL-CM5A-LR, MIROC-ESM-CHEM and MRI-CGCM3) could capture the meridional variation of the vertical easterly shear (Figure 13(b)). The greatest difference in the seasonal mean surface moisture conditions compared with ERA-interim reanalysis is the lower magnitude of specific humidity to the north of 20°N. The insufficient supply of moisture may be associated with the reduced amount of precipitation over the land region.

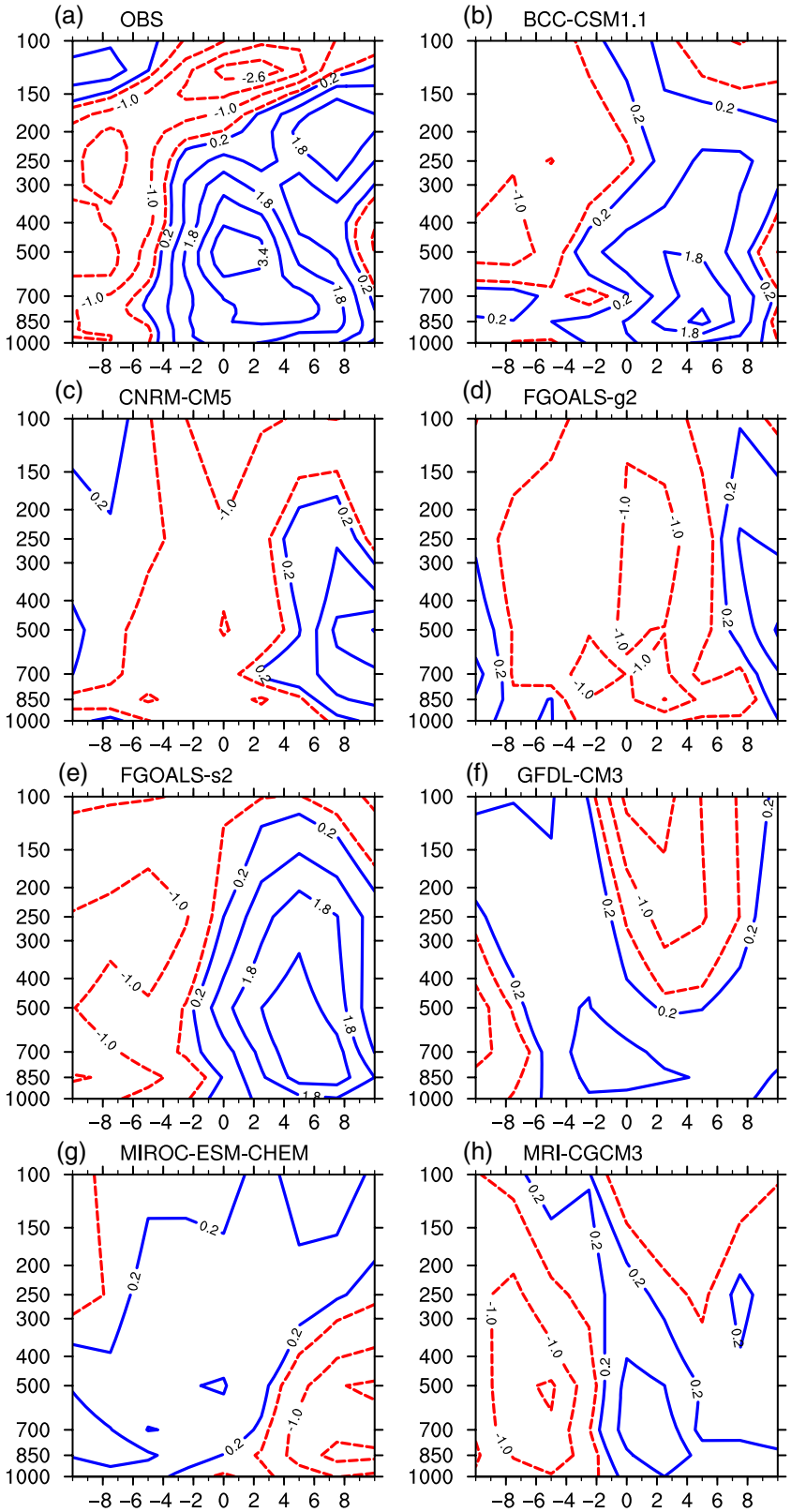

Figure 14. Meridional–vertical structures of vorticity ($10^6\,s^{-1}$) derived from ERA-interim reanalysis and model data for seven coupled models (a–h) with respect to rainfall maxima (GPCP and model precipitation) on the ISO timescales during boreal summer (May–October) in the period of 1997–2005. The horizontal axis is the meridional distance (°lat) with respect to the convection centre. A positive (negative) value means to the north (south) of the convection centre. The vertical axis is the pressure (h Pa).

However, many models with comparable vertical shear and moisture conditions have a large discrepancy in the northward propagation of the ISO (Figure 6).

Jiang *et al.* (2004) proposed that a positive vorticity perturbation with an equivalent barotropic structure appears a few latitude degrees north of the convection centre in the presence of vertical shear of the mean flow. Figure 14 shows the meridional–vertical structures of 30–80-day filtered vorticity simulated by seven of the coupled models. The horizontal axis represents the latitude distance with respect to the convection centre. Only two models (BCC-CSM1.1 and FGOALS-s2) could simulate the more accurate vertical structure of vorticity (an equivalent barotropic vorticity that occurs to the north of the convection centre). However, other models with a similar background of vertical shear produce different simulations of vorticity. Other factors may be related to the failure of reproducing the barotropic vorticity to the convection centre's north. Therefore, the mechanisms behind the northward-propagating ISO that represent the impact of atmospheric internal dynamics need to be further studied.

3.2.3. *Role of air–sea interaction*

Although some studies suggest that an AGCM is sufficient to produce the northward-propagating ISO based on the atmospheric internal dynamics, inclusion of coupling processes may further improve the simulation accuracy (Jiang *et al.*, 2004; Fu *et al.*, 2002; Fu and Wang, 2004). Here, we use the lead–lag correlation method to demonstrate the representations of air–sea interactions simulated by coupled models. Figure 15 shows the lead–lag correlations between intra-seasonal precipitation and sea surface temperature (SST) over two regions (Indian Ocean and the BOB). The results of GPCP and OISST show that the positive SST leads (lags) the positive (negative) precipitation by about 2–3 pentads, with a correlation coefficient of 0.3/0.5 (−0.3/−0.5), which passes the 95% confidence level. This indicates the main air–sea coupling process: The increasing rainfall induced by positive SST in turn decreases SST and restrains further development of convection. The phase relationship between SST and precipitation over the Indian Ocean simulated by FGOALS-s2 and HadGEM2-CC is consistent with the observations. Other models show inaccurate air–sea interactive signals. Furthermore, FGOALS-s2 simulates a more realistic phase relationship over the BOB. The accurate representation of vertical structure to the north of the convection centre (Figure 14) and the relationship between SST and precipitation simulated by FGOALS-s2 both contribute to the near-realistic simulation of the northward-propagating ISO (Figure 6).

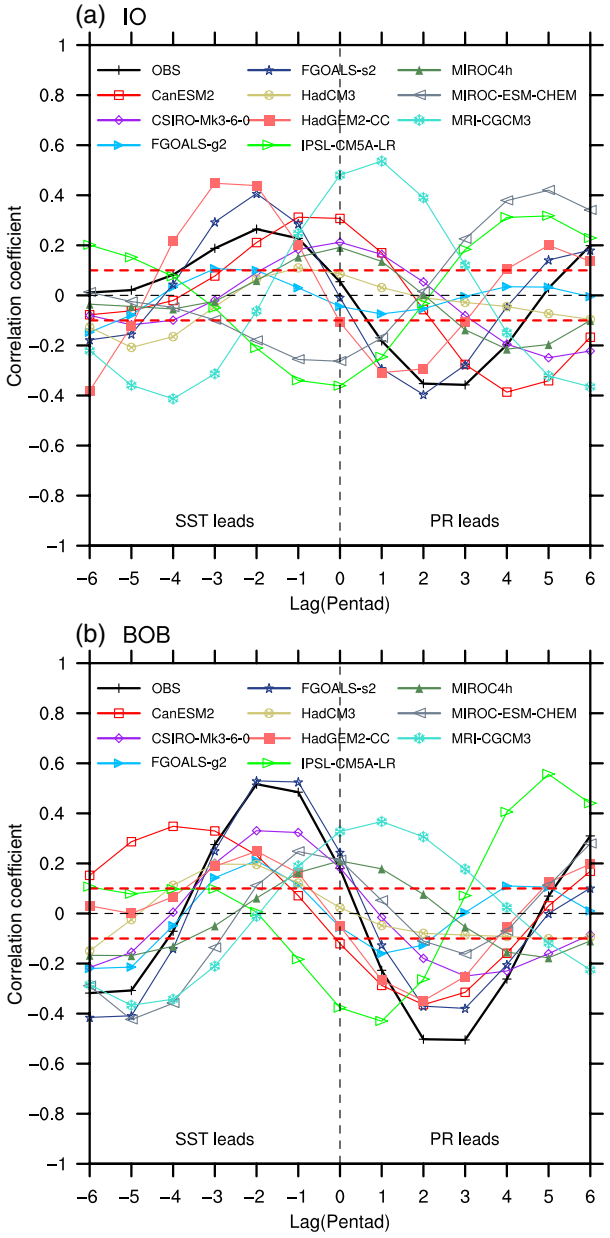

Figure 15. Lead–lag relationship between area-averaged 30 – 80-day filtered pentad rainfall (GPCP and model precipitation) with local sea surface temperature (OISST and model surface temperature), using model outputs and observational data during boreal summer (May–October) in the period of 1997–2005. The areas are over (a) the Indian Ocean (5°–10°N, 80°–90°E) and (b) the Bay of Bengal (10°–15°N, 85°–90°E). Red dashed lines represent 95% significance.

3.3. Multi-model ensemble

The multi-model ensemble (MME) not only represents the mean level of global models, but also allows us to investigate the influences of common factors in models (Weigel *et al.*, 2008; Annan and Hargreaves, 2011). Anstey *et al.* (2013) detected the role of resolution in the simulations of Northern Hemisphere winter blocking by distinguishing the CMIP5 models into four types with fine and coarse horizontal/vertical resolution. In the present study, we select adaptive models to evaluate the ensemble means of standard deviation, meridional and zonal propagation according to the four criteria described in Table 2. In brief, the ensembles are sorted on the basis of determining standards as follows: high spatial resolution (hereafter HSR; higher than 1.5° × 1.5°), low spatial resolution models (LSR; lower than 2° × 2°), high vertical re-

Table 2. Model ensembles based on four resolution criteria.

High spatial resolution (<1.5° × 1.5°)	CCSM4, CNRM-CM5, EC-EARTH, MIROC4h, MRI-CGCM3
Low spatial resolution (>2° × 2°)	CanCM4, CanESM2, FGOALS-g2, FGOALS-s2, GFDL-CM3, HadCM3, MIROC-ESM-CHEM, NorESM1-M
High vertical resolution (>L50)	EC-EARTH, MIROC4h, MIROC-ESM-CHEM
Low vertical resolution (<L30)	CCSM4, CSIRO-MK3-6-0, FGOALS-g2, FGOALS-s2, HadCM3, NorESM1-M

solution (HVR; more than 50 layers) and low vertical resolution (LVR; less than 30 layers).

Figure 16 shows the spatial distributions of standard deviation (Figures 16(a)–(d)), meridional (Figures 16(e)–(h)) and zonal (Figures 16(i)–(l)) propagations of 30–80-day ISO mode, zonal propagation of 12–24-day ISO mode (Figures 16(m)–(p)) derived from the MME mean according to the four criteria mentioned above. The corresponding observations are given in Figures 2(a), 6(a), 7(a) and 8(a). First, the pattern of standard deviation and percent variance presented by MME mean of HSR is closer to the observed than that of LSR(Figure 16(a) *vs* Figure 2(a)), which implies that improving the horizontal resolution may be associated with accurate simulation of the variance distribution in models. However, there is no distinct difference in pattern of standard deviation and percent variance between HVR and LVR (Figures 16(c) and (d)), which has stronger percent variance in the BOB and SCS than in the observed. This probably indicates that more accurate vertical divisions do not represent more reliable simulations of the ISO variance, which might be confined by other factors (such as cumulus schemes). Second, most of the coupled models can simulate the northward-propagating signals of 30–80-day ISO mode over the Asian summer monsoon region relatively well regardless of the horizontal/vertical resolution (Figures 16(e)–(h) *vs* Figure 6(a)). Third, improving horizontal or vertical resolution does not play a significant role in simulating the eastward propagation features of 30–60-day ISO mode in the off-equatorial regions (Figures 16(i)–(l) *vs* Figure 7(a)). Two models (GFDL_CM3 and IPSL-CM5A-LR) are able to capture relatively accurate characteristics of eastward propagation (Section 3.1) and these belong to the LSR and LVR categories. Fourth, models in all the categories could simulate the westward propagation of 12–24-day ISO mode in the WNP (Figures 16(m)–(p) *vs* Figure 8(a)).

Next, we evaluate the ratio between the eastward and westward variance in 30–80-day ISO mode and the ratio between the variance of westward 12–24-day mode and that of its eastward counterpart derived from MME mean according to the four criteria (Figure 17, averaged area selection is the same as in Figures 9 and 10). Figure 17(a) shows the ratio of eastward to westward components of 30–80-day ISO mode is smaller than 1 in all of four categories, whereas the ratio of the observation is approximately 2.25. The ratio by HVR models is the smallest. The ratio of westward to eastward components of 12–24-day ISO mode is given in Figure 17(b). The value of HSR, LSR and LVR is very close to the observed, approximately 2. However, the value of HVR is about two times that in the observed. Therefore, it may indicate that increasing the vertical resolution is not helpful to simulate eastward propagation of 30–80-day ISO mode and has a risk in overestimate the variance of westward component of 12–24-day ISO mode.

4. Summary and discussion

The intra-seasonal oscillation associated with Asian summer monsoon simulated by IPCC AR5 coupled models are evaluated systematically and results show that the models display a wide range of different simulation capacities. During the boreal summer, a reasonable pattern of seasonal mean rainfall over the ISM region could be reproduced by most of the IPCC AR5 climate models. However, most of models simulate insufficient precipitation over the BOB and WNPSM region and fail to produce the northeast–southwest-tilted rain belt in the EASM region. Most of the models underestimate the standard deviation of 12–90-day ISO mode over the eastern Arabian Sea, BOB and SCS, whereas most of the models overestimate the percent variance of 12–90-day ISO accounting for raw precipitation anomalies which is larger than 40% in the above areas.

The 9-summer average power spectra of the unfiltered precipitation anomalies derived from GPCP show spectral peaks in 40-day and 20-day over the NIO and WNP, respectively. As for model simulations, five models (BNU-ESM, GFDL-CM3, MIROC-ESM-CHEM, MRI-CGCM3 and NorESM1-M) could simulate two significant spectral peaks within low-frequency and quasi-biweekly periods in the NIO. Ten models (BCC-CSM1.1, CNRM-CM5, CSIRO-MK3-6-0, EC-EARTH, HadCM3, HadGEM2-CC, MIROC4h, MPI-ESM-LR, MRI-CGCM3 and NorESM1-M) could simulate the peak within the quasi-biweekly period similar to the observed in the WNP.

The characteristics of ISO propagation are examined by the point-based lead–lag correlation technique. Results show that there remains a wide gap between model simulations and observations in the simulations of eastward-propagating ISO (30–80-day) (Figure 7). Only two models could capture the features moving eastward from 40° to 120°E and westward in WNP region. Nevertheless, most of models could briefly capture the features of both northward propagation of 30–80-day mode (Figure 6) and westward propagation of 12–24-day mode (Figure 8).

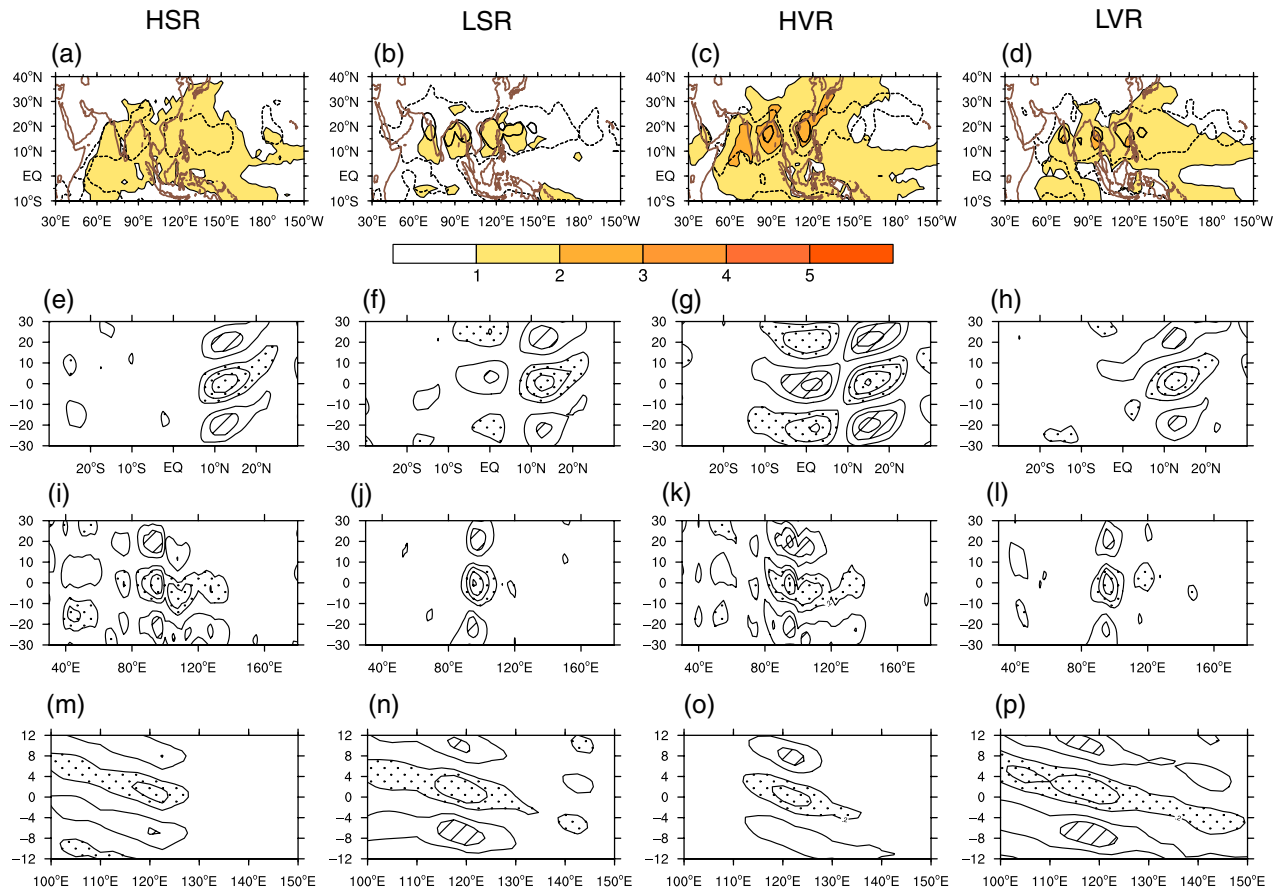

Figure 16. Spatial distributions of standard deviation and percent variance, lag-latitude and lag-longitude cross-sections derived from multi-model ensemble (MME) mean according to four criteria: (a), (e), (i) and (m) high spatial resolution (HSR; $<1.5° \times 1.5°$), (b), (f), (j) and (n) low spatial resolution (LSR; $>2° \times 2°$), (c), (g), (k) and (o) high vertical resolution (HVR; >L50) and (d), (h), (l) and (p) low vertical resolution (LVR; <L30) during boreal summer (May–October) in the period of 1997–2005. The corresponding results from GPCP and ERA-interim reanalysis are given in Figures 2(a), 6(a), 7(a) and 8(a).

Based on the mechanisms proposed by previous studies, we compare the possible factors (background circulation, atmospheric internal dynamics and ocean–atmosphere interaction) that may contribute to the propagation of the ISO. The local Hadley and Walker cell bias relates well with the model biases of moisture convergence, which will cause a local precipitation bias in models (Wang *et al.*, 2006; Goswami *et al.*, 2014). The coupled models are able to reproduce the descending branch in the Southern Hemisphere of Hadley circulation rather than the ascending branches near the equator and over the monsoon region (Figure 11). Almost all the models simulate the ascending branch over the Great Warm Pool. However, some models exaggerate the upward motions to the west of 80°E along the latitude band of 10°S–10°N. Within the similar background of vertical easterly shear (Figure 13(b)), few models have the capacity to simulate the equivalent barotropic vorticity to the north of the convection centre. Over the Indian Ocean and the BOB, the strong air–sea interaction is difficult to reproduce for many models. However, for FGOALS-s2, the combination of proper simulations of atmospheric internal dynamics and relationship between SST and precipitation may be related to a reasonable reproduction of the northward-propagating ISO.

Furthermore, the possible influences of horizontal and vertical resolution on the ISO associated with Asian summer monsoon are examined by distinguishing the CMIP5 models into higher and lower horizontal/vertical resolution. Simply improving model resolution could not be considered an effective way to obtain more accurate or clear propagation characteristics of ISO, especially for eastward propagation. This approach may combine with the selection and improvement of physical schemes to improve the simulation capacity. Nevertheless, we found that increasing spatial resolution substantially improves the capability of models to simulate spatial distribution of variance in boreal summer.

The vertical structure of mean flow in boreal summer (vertical easterly shear) is considered to be a vital factor in inducing the northward propagation of the convection centre (Jiang *et al.*, 2004). However, the analyses above demonstrate that in the model simulations, the excellent performance of simulating the vertical easterly shear is not enough to produce the northward propagation. Other elements (cumulus parameterization, air–sea coupling processes, etc.) are likely to play an important role in ISO simulation. As shown in Figures 11 and 12, the model biases in simulating the ascending branches of Hadley and

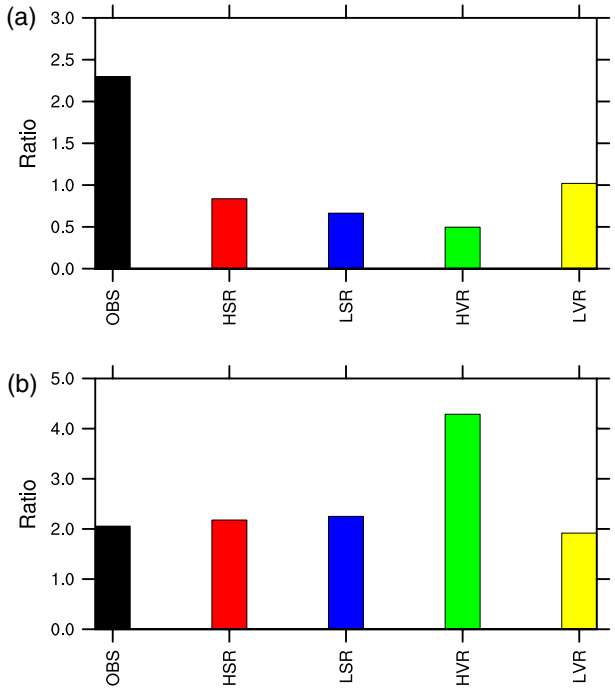

Figure 17. (a) The ratio between the variance of eastward-propagating ISO and that of its westward counterpart (30–80-day ISO mode) and (b) the ratio between the variance of westward 12–24-day mode and that of its eastward counterpart derived from the MME mean according to the four resolution criteria during boreal summer (May–October) in the period of 1997–2005 derived from GPCP and model precipitation.

Walker circulation may be related to the poor representations of moisture conditions and convection development. Furthermore, although air–sea interaction is contained in all the models, most of the models present an incorrect simulation of phase relationship between precipitation and SST. For applications other than simply solving the problems of variable exchange between ocean and atmosphere, increasing coupling frequency is necessary for reasonable simulation, because most coupled models only exchange air–sea fluxes once every 24 h. Hu *et al.* (2015) pointed out if the model adopts more frequent coupling (10 min), it is more capable of producing the eastward-propagating ISO associated with the Asian summer monsoon. This suggests that air–sea interaction may be the most essential factor with respect to the eastward-propagating component, which explains why models have such a poor capacity to simulate the eastward propagation of the ISO. Moreover, Lee *et al.* (2013) proposed two real-time indices of ISO in boreal summer, which can be used to evaluate models in another way. We will utilize them to examine ISO simulation capacities in the future study.

Acknowledgements

The authors thank the editor and two anonymous reviewers. This work is jointly supported by National Key Basic Research Program of China grants (2015CB453202 and 2014CB953902), the Strategic Leading Science Projects of the Chinese Academy of Sciences (Grant XDA11010402), National Natural Science Foundation of China grants (41305065, 91337216 and 41305068) and the Open Project of the Key Laboratory of Meteorological Disaster of the Ministry of Education (KLME1503).

References

Ajayamohan RS, Goswami BN. 2007. Dependence of simulation of summer tropical intraseaaonsal oscillations on the simulation of seasonal mean. *J. Atmos. Sci.* **64**: 460–478.
Annan JD, Hargreaves JC. 2011. Understanding the CMIP3 multimodel ensemble. *J. Clim.* **24**: 4529–4538.
Anstey JA, Davini P, Gray LJ, Woollings TJ, Butchart N, Cagnazzo C, Christiansen B, Hardiman SC, Osprey SM, Yang ST. 2013. Multi-model analysis of Northern Hemisphere winter blocking: model biases and the role of resolution. *J. Geophys. Res.* **118**: 3956–3971.
Arakawa A, Schubert WH. 1974. Interactions of cumulus cloud ensemble with the large-scale environment, Part I. *J. Atmos. Sci.* **31**: 674–701.
Bougeault P. 1985. A simple parameterization of the large-scale effects of cumulus convection. *Mon. Weather Rev.* **113**: 2108–2121.
Chen TC, Chen JM. 1995. An observational study of the South China Sea monsoon during the 1979 summer: onset and life cycle. *Mon. Weather Rev.* **123**: 2295–2318.
Chen TC, Yen MC, Weng SP. 2000. Interaction between the summer monsoons in East Asia and the South China Sea: intraseasonal monsoon modes. *J. Atmos. Sci.* **57**: 1373–1392.
Chikira M, Sugiyama M. 2010. A cumulus parameterization with state-dependent entrainment rate. Part I. Description and sensitivity to temperature and humidity profiles. *J. Atmos. Sci.* **67**: 2171–2193.
Dee DP, Uppala SM, Simmons AJ, Berrisford P, Poli P, Kobayashi S, Andrae U, Balmaseda MA, Balsamo G, Bauer P, Bechtold P, Beljaars ACM, van de Berg L, Bidlot J, Bormann N, Delsol C, Dragani R, Fuentes M, Geer AJ, Haimberger L, Healy SB, Hersbach H, Hólm EV, Isaksen L, Kållberg P, Köhler M, Matricardi M, McNally AP, Monge-Sanz BM, Morcrette J-J, Park B-K, Peubey C, de Rosnay P, Tavolato C, Thépaut J-N, Vitart F. 2011. The ERA-interim reanalysis: configuration and performance of the data assimilation system. *Q. J. R. Meteorol. Soc.* **137**: 553–597.
Derbyshire SH, Maidens AV, Milton SF, Stratton RA, Willett MR. 2011. Adaptive detrainment in a convective parametrization. *Q. J. R. Meteorol. Soc.* **137**: 1856–1871.
Duchon CE. 1979. Lanczos filtering in one and two dimensions. *J. Appl. Meteorol.* **18**: 1016–1022.
Emanuel KA. 1991. A scheme for representing cumulus convection in large-scale models. *J. Atmos. Sci.* **48**: 2313–2335.
Emori S, Nozawa T, Numaguchi A, Uno I. 2001. Importance of cumulus parameterization for precipitation simulation over East Asia in June. *J Meteorol Soc Jpn* **79**: 939–947.
Fritsch JM, Chappell CG. 1980. Numerical prediction of convectively driven mesoscale pressure systems. Part I. Convective parametrization. *J. Atmos. Sci.* **37**: 1722–1733.
Fu X, Wang B. 2004. Differences of boreal summer intraseasonal oscillations simulated in an atmosphere–ocean coupled model and an atmosphere-only model. *J. Clim.* **17**: 1263–1271.
Fu X, Wang B, Li T. 2002. Impacts of air–sea coupling on the simulation of the mean Asian summer monsoon in the ECHAM4 model. *Mon. Weather Rev.* **130**: 2889–2903.
Gilman DL, Fuglister FJ, Mitchell JM Jr. 1963. On the power spectrum of "red noise". *J. Atmos. Sci.* **20**: 182–184.
Goswami BN. 2005. In *South Asian monsoon: intraseasonal variability of the atmosphere–ocean climate system*, Lau WKM, Waliser DE (eds). Springer, 36.
Goswami BB, Deshpande M, Mukhopadhyay P, Saha SK, Rao SA, Raghu Murthugudde R, Goswami BN. 2014. Simulation of monsoon intraseasonal variability in NCEP CFSv2 and its role on systematic bias. *Clim. Dyn.* **43**: 2725–2745.
Grabowski WW. 2003. MJO-like coherent structures: sensitivity simulations using the Cloud-Resolving Convection Parameterization (CRCP). *J. Atmos. Sci.* **60**: 847–864.
Gregory D, Kershaw R, Inness PM. 1997. Parametrisation of momentum transport by convection II: tests in single column and general circulation models. *Q. J. R. Meteorol. Soc.* **123**: 1153–1183.

Hartmann DL, Michelsen ML, Klein SA. 1992. Seasonal variations of tropical intraseasonal oscillations: a 20–25 day oscillation in the western pacific. *J. Atmos. Sci.* **49**: 1277–1289.
Hsu HH, Weng CH. 2001. Northwestward propagation of the intraseasonal oscillation in the western North Pacific during the boreal summer: structure and mechanism. *J. Clim.* **14**: 3834–3850.
Hu WT, Duan AM, Wu GX. 2011. Sensitivity of simulated tropical intraseasonal oscillations to cumulus schemes. *Sci. China Earth Sci.* **54**: 1761–1771, doi: 10.1007/s11430-011-4215-0.
Hu WT, Duan AM, Wu GX. 2015. Impact of subdaily air–sea interaction on simulating intraseasonal oscillations over the Tropical Asian Monsoon Region. *J. Clim.* **28**: 1057–1073.
Huang P, Chou C, Huang R. 2011. Seasonal modulation of tropical intraseasonal oscillations on tropical cyclone genesis in the western North Pacific. *J. Clim.* **24**: 6339–6352.
Huffman GJ, Adler RF, Morrissey MM, Curtis S, Joyce R, McGavock B, Susskind J. 2001. Global precipitation at one-degree daily resolution from multisatellite observations. *J. Hydrometeor.* **2**: 36–50.
Inness PM, Slingo JM, Woolnough SJ, Neale RB, Pope VD. 2001. Oragnization of tropical convection in a GCM with varying vertical resolution; implications for the simulation of the Madden-Julian oscillation. *Clim. Dyn.* **17**: 777–793.
Jiang XA, Li T, Wang B. 2004. Structures and mechanisms of the northward propagating boreal summer intraseasonal oscillation. *J. Clim.* **17**: 1022–1039.
Ju JH, Zhao EX. 2005. Impacts of the low frequency oscillation in East Asian summer monsoon on the drought and flooding in the middle and lower valley of Yangtze River. *J. Trop. Meteorol.* **2**: 163–171.
Kemball-Cook S, Wang B. 2001. Equatorial waves and air–sea interaction in the Boreal summer intraseasonal oscillation. *J. Clim.* **14**: 2923–2942.
Kiladis GN, Weickmann KM. 1997. Horizontal structure and seasonality of large-scale circulations associated with submonthly tropical convection. *Mon. Weather Rev.* **125**: 1997–2013.
Krishnamurti TN, Ardunay P. 1980. The 10 to 20 day westward propagating mode and "breaks" in the monsoons. *Tellus* **32**: 15–26.
Krishnamurti TN, Subrahmanyam D. 1982. The 30–50 day mode at 850 Mb during MONEX. *J. Atmos. Sci.* **39**: 2088–2095.
Lau KH, Lau NC. 1990. Observed structure and propagation characteristics of tropical summertime synoptic scale disturbances. *Mon. Weather Rev.* **118**: 1888–1913.
Lawrence DM, Webster PJ. 2002. The boreal summer intraseasonal oscillation: relationship between Northward and Eastward movement of convection. *J. Atmos. Sci.* **59**: 1593–1606.
Lee J, Wang B, Wheeler MC, Fu X, Waliser DE, Kang I. 2013. Real-time multivariate indices for the boreal summer intraseasonal oscillation over the Asian summer monsoon region. *Clim. Dyn.* **40**: 493–509.
Liebmann B, Hendon HH, Glick JD. 1994. The relationship between tropical cyclones of the western Pacific and Indian Oceans and the Madden–Julian oscillation. *J. Meteorol. Soc. Jpn.* **72**: 401–411.
Lin JL, Weickman KM, Kiladis GN, Mapes BE, Schubert SD, Suarez MJ, Bacmeister JT, Lee M-I. 2008. Subseasonal variability associated with Asian summer monsoon simulated by 14 IPCC AR4 coupled GCMs. *J. Clim.* **21**: 4541–4567.
Maloney ED, Hartmann DL. 2000. Modulation of eastern North Pacific hurricanes by the Madden-Julian oscillation. *J. Clim.* **13**: 1451–1460.
Maloney ED, Hartmann DL. 2001. The sensitive of intraseasonal variability in the NCAR CCM3 to changes in convection parameterization. *J. Clim.* **14**: 2015–2034.
Mao JY, Chan JCL. 2005. Intraseasonal variability of the South China Sea summer monsoon. *J. Clim.* **18**: 2388–2402.
Moorthi S, Suarez MJ. 1992. Relaxed Arakawa–Schubert: a parameterization of moist convection for general circulation models. *Mon. Weather Rev.* **120**: 978–1002.
Murakami T. 1980. Empirical orthogonal function analysis of satellite-observed outgoing longwave radiation during summer. *Mon. Weather Rev.* **108**: 205–222.
Nordeng TE. 1994. Extended versions of the convection parametrization scheme at ECMWF and their impact upon the mean climate and transient activity of the model in the tropics. ECMWF Tech. Memo. No. 206.
Pan DM, Randall DA. 1998. A cumulus parameterization with a prognostic closure. *Q. J. R. Meteorol. Soc.* **124**: 949–981.
Randall D, Khairoutdinov M, Arakawa Akio A, Grabowski W. 2003. Nreaking in the cloud parameterization deadlock. *Bull. Am. Meteorol. Soc.* **84**: 1547–1564.
Reynolds RW, Rayner NA, Smith TM, Stokes DC, Wang W. 2002. An improved in situ and satellite SST analysis for climate. *J. Clim.* **15**: 1609–1625.
Sabeerali CT, Ramu Dandi A, Dhakate A, Salunke K, Mahapatra S, Rao SA. 2013. Simulation of boreal summer intraseasonal oscillations in the latest CMIP5 coupled GCMs. *J. Geophys. Res. Atmos.* **118**: 4401–4420, doi: 10.1002/jgrd.50403.
Sikka DR, Gadgil S. 1980. On the maximum cloud zone and the ITCZ over Indian longitude during southwest monsoon. *Mon. Weather Rev.* **108**: 1840–1853.
Silvio G, Navarra A, Storch HV. 1996. Tropical intraseasonal oscillation in operational analyses and in a family of general circulation models. *J. Atmos. Sci.* **54**: 1185–1203.
Slingo JM, Sperber KR, Boyle JS, Ceron J-P, Dix M, Dugas B, Ebisuzaki W, Fyfe J, Gregory D, Gueremy J-F, Hack J, Harzallah A, Inness P, Kitoh A, Lau WK-M, McAvaney B, Madden R, Matthews A, Palmer TN, Park C-K, Randall D, Renno N. 1996. Intraseasonal oscillation in 15 atmospheric general circulation models: results from an AMIP diagnostic subproject. *Clim. Dyn.* **12**: 325–357.
Sperber KR, Annamalai H. 2008. Coupled model simulations of boreal summer intraseasonal (30–50 day) variability. Part 1. Systematic errors and caution on use of metrics. *Clim. Dyn.* **31**: 345–372.
Sperber KR, Brankovic C, Deque M, Frederiksen CS, Graham R, Kitoh A, Kobayashi C, Palmer T, Puri K, Tennant W, Volodin E. 2001. Dynamical seasonal predictability of the Asian summer monsoon. *Mon. Weather Rev.* **129**: 2226–2248.
Straub KH, Kiladis GN. 2003. Interactions between the boreal summer intraseasonal oscillation and higher-frequency tropical wave activity. *Mon. Weather Rev.* **131**: 945–960.
Tiedtke M. 1989. A comprehensive mass flux scheme for cumulus parameterization in large-scale models. *Mon. Weather Rev.* **117**: 1779–1800.
Waliser DE, Jin K, Kang I-S, Stern WF, Schubert SD, Lau K-M, Lee M-I, Krishnamurthy V, Kitoh A, Meehl GA, Galin VY, Satyan V, Mandke SK, Wu G, Liu Y, Park C-K. 2003. AGCM simulations of intraseasonal variability associated with the Asian Summer Monsoon. *Clim. Dyn.* **21**: 423–446.
Wang B, Rui H. 1990. Synoptic climatology of transient tropical intraseasonal convection anomalies: 1975–1985. *Meteor. Atmos. Phys.* **44**: 43–61.
Wang B, Webster P, Kikuchi K, Yasunari T, Qi Y. 2006. Boreal summer quasi-monthly oscillation in the global tropics. *Clim. Dyn.* **27**: 661–675.
Weigel AP, Liniger MA, Appenzeller C. 2008. Can multi-model combination really enhance the prediction skill of probabilistic ensemble forecasts? *Q. J. R. Meteorol. Soc.* **134**: 241–260.
Wheeler M, Kiladis GN. 1999. Convectively coupled equatorial waves: analysis of clouds and temperature in the wave-number-frequency domain. *J. Atmos. Sci.* **56**: 374–399.
Wu R. 2010. Subseasonal variability during the South China Sea summer monsoon onset. *Clim. Dyn.* **34**: 629–642.
Yasunari T. 1979. Cloudiness fluctuations associated with the Northern Hemisphere summer monsoon. *J. Meteorol. Soc. Jpn.* **57**: 227–242.
Yasunari T. 1980. A quasi-stationary appearance of the 30–40 day period in the cloudiness fluctuations during the summer monsoon over India. *J. Meteorol. Soc. Jpn.* **59**: 336–354.
Zhang GJ, McFarlane NA. 1995. Sensitivity of climate simulations to the parameterization of cumulus convection in the CCC-GCM. *Atmosphere–Ocean* **3**: 407–446.
Zhang GJ, Mu M. 2005. Effects of modifications to the Zhang-McFarlane convection parameterization on the simulation of the tropical precipitation in the National Center for Atmospheric Research Community Climate Model, version 3. *J. Geophys. Res.* **110**: D09109, doi: 10.1029/2004JD005617.
Zhang C, Dong M, Hendon HH, Maloney ED, Marshall A, Sperber KR, Wang W. 2006. Simulations of the Madden-Julian oscillation in four pairs of coupled and uncoupled global models. *Clim. Dyn.* **27**(6): 573–592, doi: 10.1007/s00382-006-0148-2.
Zhu CW, Nakazawa T, Li JP. 2003. The 30–60 day intraseasonal oscillation over the western North Pacific Ocean and its impacts on summer flooding in China during 1998. *Geophys. Res. Lett.* **30**: 1952.

